[20] Snell PG, Martin WH, Buckey JC, Blomqvist CG. Maximal vascular leg conductance in trained and untrained men. J Appl Physiol 1987; 62:606–10.

[21] Logan J, Fowler JS, Volkow ND, Wolf AP, Dewey SL, Schlyer DJ, et al. Graphical analysis of reversible radioligand binding from time–activity measurements applied to [N-^{11}C-methyl]-(−)-cocaine PET studies in human subjects. J Cereb Blood Flow Metab 1990; 10:740–7.

[22] Kawakami Y, Nakazawa K, Fujimoto T, Nozaki D, Miyashita M, Fukunaga T. Specific tension of elbow flexor and extensor muscles based on magnetic resonance imaging. Eur J Appl Physiol 1994;68: 139–47.

[23] Dixon AK, Gubitz AK, Sirinathsinghji DJ, Richardson PJ, Freeman TC. Tissue distribution of adenosine receptor mRNAs in the rat. Br J Pharmacol 1996;118:1461–8.

[24] Allard MF, Kamimura CT, English DR, Henning SL, Wiggs BR. Regional myocardial capillary erythrocyte transit time in the normal resting heart. Circ Res 1993;72:187–93.

[25] Diffee GM, Nagle DF. Regional differences in effects of exercise training on contractile and biochemical properties of rat cardiac myocytes. J Appl Physiol 2003;95:35–42.

[26] Zhang C, Hein TW, Kuo L. Transmural difference in coronary arteriolar dilation to adenosine: effect of luminal pressure and KATP channels. Am J Physiol 2000;79:H2612–9.

[27] Kalliokoski KK, Nuutila P, Laine H, Luotolahti M, Janatuinen T, Raitakari OT, et al. Myocardial perfusion and perfusion reserve in endurance-trained men. Med Sci Sports Exerc 2002;34:948–53.

[28] Lynge J, Hellsten Y. Distribution of adenosine A_1, A_{2A} and A_{2B} receptors in human skeletal muscle. Acta Physiol Scand 2000;169:283–90.

[29] Honig CR, Odoroff CL, Frierson JL. Capillary recruitment in exercise: rate, extent, uniformity, and relation to blood flow. Am J Physiol 1980; 238:H31–H42.

[30] Kalliokoski KK, Oikonen V, Takala TO, Sipila H, Knuuti J, Nuutila P. Enhanced oxygen extraction and reduced flow heterogeneity in exercising muscle in endurance-trained men. Am J Physiol 2001;280: E1015–21.

[31] Knuuti J, Nuutila P. PET as a cardiovascular and metabolic research tool. Ann Med 1999;31:450–6.

[32] Nuutila P, Kalliokoski K. Use of positron emission tomography in the assessment of skeletal muscle and tendon metabolism and perfusion. Scand J Med Sci Sports 2000;10:346–50.

[33] Mizuno M, Kimura Y, Iwakawa T, Oda K, Ishii K, Ishiwata K, et al. Regional differences in blood volume and blood transit time in resting skeletal muscle. Jpn J Physiol 2003;53:467–70.

[34] Mizuno M, Kimura Y, Iwakawa T, Oda K, Ishii K, Ishiwata K, et al. Regional differences in blood flow and oxygen consumption in resting muscle and their relationship during recovery from exhaustive exercise. J Appl Physiol 2003;95:2204–10.

Adenosine A_1 Receptor Mapping of the Human Brain by PET with 8-Dicyclopropylmethyl-1-^{11}C-Methyl-3-Propylxanthine

Nobuyoshi Fukumitsu, MD[1,2]; Kenji Ishii, MD[1]; Yuichi Kimura, PhD[1]; Keiichi Oda, PhD[1]; Toru Sasaki, PhD[1]; Yutaka Mori, MD, PhD[3]; and Kiichi Ishiwata, PhD[1]

[1]*Positron Medical Center, Tokyo Metropolitan Institute of Gerontology, Tokyo, Japan;* [2]*Proton Medical Research Center, University of Tsukuba, Ibaragi, Japan; and* [3]*Department of Radiology, Jikei University School of Medicine, Tokyo, Japan*

Adenosine is an endogenous modulator of synaptic functions in the central nervous system. To investigate the physiologic and pathologic roles of the adenosine receptors in the human brain, PET is a powerful in vivo technique. In this study, we quantitatively evaluated the distribution of a major subtype A_1 adenosine receptor in the human brain by PET with a newly developed radioligand, 8-dicyclopropylmethyl-1-^{11}C-methyl-3-propylxanthine (^{11}C-MPDX). **Methods:** In 5 healthy volunteers, after PET measurement of the regional cerebral blood flow (rCBF) with ^{15}O-H_2O, a 60-min PET scan with ^{11}C-MPDX was performed. The distribution volume (DV) of ^{11}C-MPDX was quantitatively evaluated by Logan's graphical analysis. **Results:** ^{11}C-MPDX was taken up at a high level, reaching a peak at 2–2.5 min, followed by a rapid decrease. The unchanged form of ^{11}C-MPDX in plasma was 75% at 60 min after injection. The DV of ^{11}C-MPDX was large in the striatum and thalamus, moderate in the cerebral cortices and pons, and small in the cerebellum. The distribution pattern of ^{11}C-MPDX in the brain was coincident with that of adenosine A_1 receptors in vitro, reported previously, but discretely different from that of rCBF. **Conclusion:** ^{11}C-MPDX PET has the potential for mapping adenosine A_1 receptors in the human brain.

Key Words: 8-dicyclopropylmethyl-1-^{11}C-methyl-3-propylxanthine; adenosine A_1 receptor; brain; PET

J Nucl Med 2005; 46:32–37

Adenosine is present in large amounts in the mammalian brain and plays a role as an endogenous modulator of synaptic functions in the central nervous system. The effects are mediated by at least 4 adenosine receptor subtypes: A_1, A_{2A}, A_{2B}, and A_3. The 2 major subtypes of receptors—A_1 and A_2 receptors—have been investigated well in molecular biology, pharmacology, and physiology (*1–3*). The adenosine A_1 receptors exhibit a high affinity for adenosine and inhibit adenylyl cyclase. It is now known that A_1 receptors are G protein linked and can act through effectors other than adenylyl cyclase, including potassium channels, calcium channels, phospholipase A_2 and C, and guanylyl cyclase (*1*).

Previous work has established a role for adenosine in a diverse array of neural phenomena, which include regulation of sleep and the level of arousal, neuroprotection, regulation of seizure susceptibility, locomotor effects, analgesia, mediation of the effects of ethanol, and chronic drug use (*4*). They are mediated by both adenosine A_1 and A_{2A} receptors. Therefore, interaction with adenosine metabolism is a promising target for therapeutic intervention in ischemic brain disorders, neurologic and psychiatric diseases such as epilepsy, sleep, movement (parkinsonism or Huntington's disease), or psychiatric disorders (Alzheimer's disease, depression, schizophrenia, or addiction) (*3,5,6*).

For the purpose of mapping adenosine A_1 and A_{2A} receptors in the brain by PET, we synthesized and characterized several radioligands (*7,8*). Recently we performed imaging of adenosine A_1 receptors in the human brain by PET with 8-dicyclopropylmethyl-1-^{11}C-methyl-3-propylxanthine (^{11}C-MPDX) (Fig. 1) (*9*) following the developmental studies with animals (*7,10–15*). Bauer et al. also reported the mapping of adenosine A_1 receptors in the human brain by PET with a xanthine-type analog, 8-cyclopentyl-3-(3-^{18}F-fluoropropyl)-1-propylxanthine (^{18}F-CPFPX) (*16*). In this study, we quantitatively evaluated the distribution volume (DV) of ^{11}C-MPDX in the brain of healthy volunteers by a graphical analysis method.

MATERIALS AND METHODS

The study protocol was approved by the Institutional Ethical Committee. Five male volunteers (age, 21.6 ± 1.5 y old; age range, 20–24 y old; body weight, 62.4 ± 2.3 kg; body weight range, 59–64 kg) participated in this study, and written informed consent was obtained from the subjects. All subjects were healthy according to the history, physical, neurologic, and psychiatric examinations, and MRI study of the brain before the PET study.

Received Mar. 18, 2004; revision accepted Aug. 12, 2004.

For correspondence or reprints contact: Nobuyoshi Fukumitsu, MD, Proton Medical Research Center, University of Tsukuba, 1-1-1, Tennoudai, Ibaragi, 305-8575, Japan.

E-mail: GZL13162@nifty.ne.jp

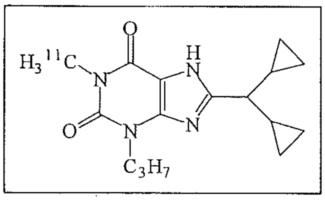

FIGURE 1. Chemical structure of ^{11}C-MPDX.

Radiosynthesis of ^{11}C-MPDX was performed as previously described (*10,14*). The injection radioactivity dose was 611 ± 93 MBq (range, 484–700 MBq), and the mass was 15.5 ± 6.9 nmol (range, 9.9–27.5 nmol). The specific radioactivity was 43.4 ± 13.4 TBq/mmol (range, 25.5–55.6 TBq/mmol).

PET Measurement

PET measurement was performed with a SET-2400W (Shimadzu Co.), which acquires 63 slices having 128 × 128 pixels each at a transverse resolution of 4.5-mm full width of half maximum (FWHM) and at an axial resolution of 5.8-mm FWHM. Scanning took place as the subjects laid supine. A venous catheter was inserted into a forearm vein of the subjects for tracer injection, and an arterial catheter was inserted into a distal radial artery under local anesthesia for sampling arterial blood. After positioning the subject's head in the canthomeatal orientation, a transmission scan was performed with a rotating ^{68}Ga/^{68}Ge line source to correct for the photon attenuation using the attenuation map. Then, ^{15}O-H_2O (120–150 MBq) was injected intravenously into the subject for a period of 10 s, and a PET scan was performed for 120 s in a 3-dimensional static mode. Ten minutes later, after the first scan, the subject was given ^{11}C-MPDX for a period of 10 s, and the second PET scan was performed for 60 min in a 2-dimensional dynamic mode (10 s × 6 frames, 30 s × 3 frames, 60 s × 5 frames, 150 s × 5 frames, and 300 s × 8 frames). The tomographic images were reconstructed using a filtered backprojection method and Butterworth filter (cutoff frequency, 1.25 cycle/cm; order, 2). The data were collected in a 128 × 128 × 31 matrix. The voxel size was 2 × 2 × 6.25 mm.

Blood Sampling and Metabolite Analysis

Arterial blood was taken at 10, 20, 30, 40, 50, 60 70, 80, 90, 100, 110, 120, 135, and 150 s and at 3, 5, 7, 10, 15, 20, 30, 40, 50, and 60 min. The whole blood and plasma were measured for radioactivity with a γ-counter and weighed. The time–activity curves were expressed as becquerels per milliliter or the standardized uptake value (SUV) (grams body weight × Bq/mL tissue/total injected dose). The unchanged form of ^{11}C-MPDX in the plasma sampled at 3, 10, 20, 30, 40, and 60 min was analyzed by high-performance liquid chromatography (HPLC) as described (*10*).

Kinetic Analysis

PET images were registrated and resliced to MRI with the Ardekani image registration algorithm (*17*) by UNIX workstations (Silicon Graphics Inc.) using the Dr. View image analysis software system (Asahi Kasei Joho System). Regions of interest (ROIs) were placed on the frontal, medial frontal, temporal, medial temporal, parietal, and occipital cortices, striatum, thalamus, cerebellum, and pons based on MRI. The ROI in the frontal cortex had 835 voxels and that in the pons had 87 voxels (1 pixel = 2 × 2 × 6.25 mm). The pixel numbers in other regions were in-between. The regional cerebral blood flow (rCBF) was measured by the autoradiographic method (*18*). The binding of ^{11}C-MPDX was evaluated by a graphical analysis according to the method described by Logan et al. (*19*). Time–activity curves for each ROI of the brain were calculated as becquerels per milliliter or SUV. Using the time–activity curves of the brain tissues and the metabolite-corrected time–activity curve of plasma, the DV for ^{11}C-MPDX was evaluated. Equation 1 describes the concept of the Logan plot in which integrals of the elapsed-time time–activity curve and the plasma time–activity curve normalized by the elapsed-time time–activity curve have a linear relationship and its gradient derives a total DV:

$$\frac{\int_0^t ROI(t')dt'}{ROI(t)} = DV\frac{\int_0^t Cp(t')dt'}{ROI(t)} + int, \qquad \text{Eq. 1}$$

where *Cp* is activity in plasma, *t* is elapsed time, and *int* is integral. A Logan plot was applied to every voxel to make a parametric image on the DV. First, the integrated values were calculated using trapezoidal integration, and Logan plots were formed with an integrated plasma time–activity curve. Then, regression lines were estimated using the plots between 10 and 40 min after ^{11}C-MPDX injection. An estimated gradient means total DV, and an image of the DV can be obtained.

RESULTS

Figure 2 shows the time–activity curves of whole blood and plasma after injection of ^{11}C-MPDX. The SUVs of blood and plasma decreased rapidly for the first 10 min after injection and then decreased gradually. A discrepancy between 2 levels was observed on and after 10 min. The level of blood was slightly higher than that of plasma. Labeled metabolites of ^{11}C-MPDX in plasma were analyzed by HPLC. Three polar metabolites (reten-

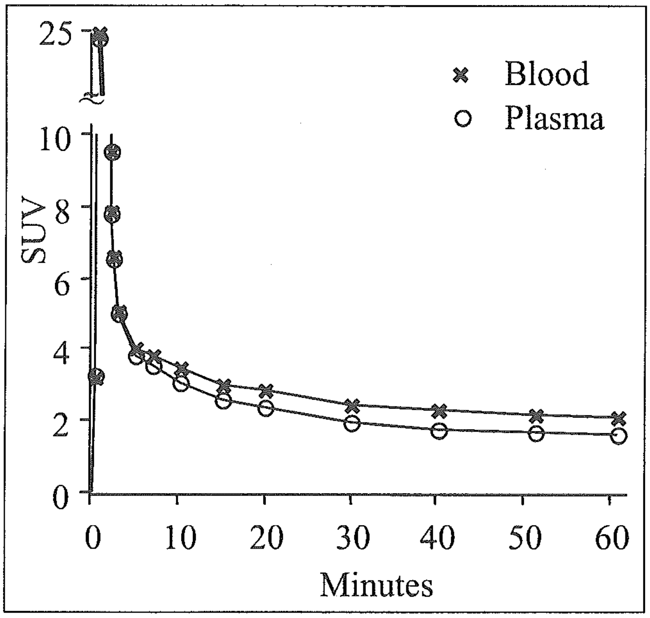

FIGURE 2. Time–activity curves in blood and plasma after injection of ^{11}C-MPDX. Data represent means of 5 subjects. SUVs of blood and plasma decreased rapidly for first 10 min after injection. SUV of blood was slightly higher than that of plasma.

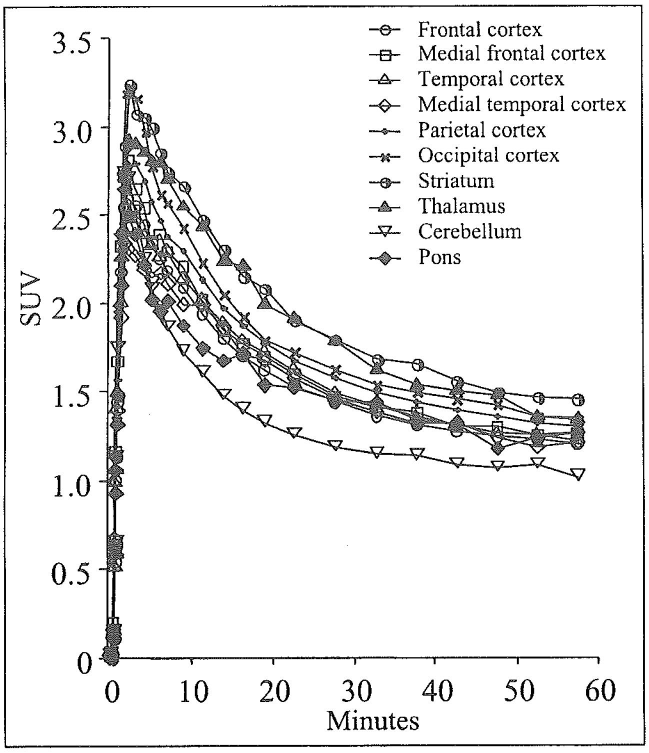

FIGURE 3. Time–activity curves in each region in brain after injection of ^{11}C-MPDX. Data represent means of 5 subjects. Uptake of ^{11}C-MPDX in each region was high, followed by rapid decrease for first 15 min. SUV was relatively high in striatum and thalamus and low in cerebellum.

tion times: 1.8, 3.2, and 4.3 min) were found in addition to ^{11}C-MPDX (retention time: 6.3 min). The unchanged form of ^{11}C-MPDX in plasma was 98.5% ± 0.64% at 3 min, 88.8% ± 2.85% at 10 min, 82.8% ± 5.38% at 20 min, 82.2% ± 8.28% at 30 min, 77.1% ± 5.38% at 40 min, and 74.9% ± 5.00% at 60 min.

Figure 3 shows the time–activity curves of each brain region after injection of ^{11}C-MPDX. ^{11}C-MPDX was taken at high levels in all regions investigated, and the uptake reached a peak at 2–2.5 min after injection, followed by a rapid decrease for the first 15 min. Approximately 6% of the total injected ^{11}C-MPDX was taken up in the brain at 2–2.5 min. The clearance patterns differed slightly among each region. The SUV was relatively high in the striatum and thalamus and low in the cerebellum.

Figure 4 shows the brain MRI and PET parametric images in a typical case. The distribution pattern of ^{11}C-MPDX was discretely different from that of rCBF. The binding of ^{11}C-MPDX was very low in the cerebellum and high in the striatum and thalamus, where the rCBF was relatively lower.

Table 1 summarizes the DV of ^{11}C-MPDX and rCBF. A typical Logan plot was shown in Figure 5. The DV was large in the striatum and thalamus, moderate in 6 cortical regions and the pons, and small in the cerebellum. The DV pattern of ^{11}C-MPDX in the brain was different from the rCBF pattern. The rCBF was low in the temporal and medial frontal cortices and pons.

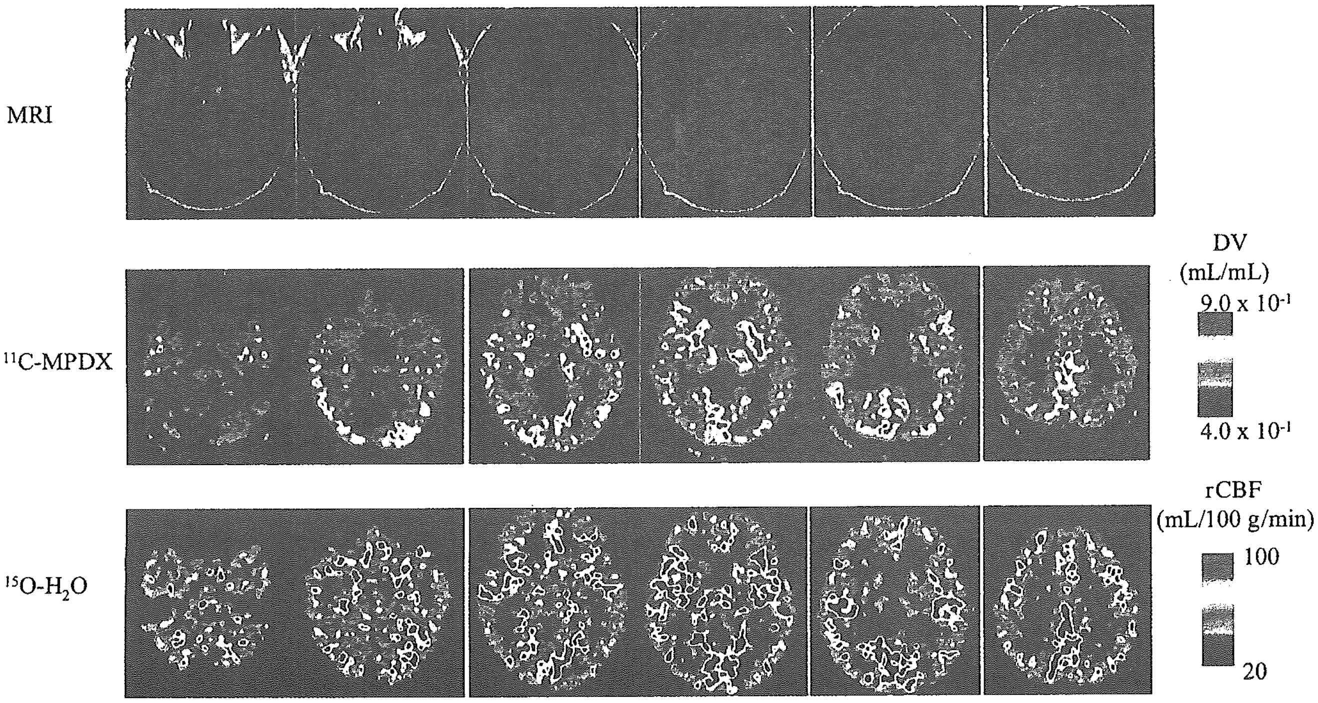

FIGURE 4. Brain MRI and PET parametric images in typical case. (Top) MRI. (Middle) Distribution image (DV) of ^{11}C-MPDX. (Bottom) rCBF with ^{15}O-H$_2$O. DV of ^{11}C-MPDX was low in cerebellum and high in striatum and thalamus, where rCBF was relatively lower.

TABLE 1
DV of ^{11}C-MPDX and rCBF in Brain Regions of Young Healthy Subjects

Brain region	DV (mL/mL)	rCBF (mL/100 g/min)
Frontal cortex	0.69 ± 0.17	59.9 ± 14.7
Medial frontal cortex	0.70 ± 0.19	65.8 ± 16.8
Temporal cortex	0.70 ± 0.19	53.9 ± 11.4
Medial temporal cortex	0.68 ± 0.18	56.3 ± 13.1
Parietal cortex	0.75 ± 0.18	65.9 ± 18.6
Occipital cortex	0.78 ± 0.21	72.4 ± 20.5
Striatum	0.84 ± 0.23	71.8 ± 23.6
Thalamus	0.81 ± 0.21	72.9 ± 23.5
Cerebellum	0.58 ± 0.14	72.0 ± 23.1
Pons	0.67 ± 0.18	60.4 ± 15.2

Data represent mean ± SD (n = 5).

DISCUSSION

Following the preclinical studies on the mapping of adenosine A_1 receptors in the brain of cats and monkeys by ^{11}C-MPDX PET (*1–15*), we performed a clinical study on ^{11}C-MPDX PET and demonstrated the potential of ^{11}C-MPDX as a radioligand for mapping adenosine A_1 receptors in the human brain (*9*). In the present study, we quantitatively evaluated the binding of ^{11}C-MPDX in the brain of healthy subjects.

In the literature, the adenosine A_1 receptors are rich in the hippocampus, cerebral cortex, thalamic nuclei, and basal ganglia of the postmortem human brain (*16,20,21*). In the cerebral cortex, the adenosine A_1 receptors were rich in primary visual cortex layer III in the occipital cortex and superficial and intermediate layers in the parietal cortex. On the other hand, the density was relatively low in the frontal, temporal, and cingulate cortices. In the present PET study, the binding of ^{11}C-MPDX evaluated quantitatively as the DV was relatively higher in the striatum and thalamus among the brain regions investigated and lower in the cerebellum. In the cerebral cortex, the DV was relatively larger in the occipital and parietal cortices and smaller in the frontal and temporal cortices. The DV pattern of ^{11}C-MPDX in vivo was consistent with that of the A_1 receptor in vitro represented in previous reports (*20–24*), demonstrating that ^{11}C-MPDX is a suitable radioligand for mapping adenosine A_1 receptors.

In the present study, we did not directly certify the specific binding of ^{11}C-MPDX to the adenosine A_1 receptors by blocking studies. However, we previously confirmed the A_1 receptor-specific binding of ^{11}C-MPDX in animals. Coinjection of unlabeled MPDX or A_1-selective KF15372 significantly blocked the brain uptake in mice, rats, and cats (*10–13*). In a PET study with cats, the reversible binding of ^{11}C-MPDX was clearly demonstrated after treatment with A_1-selective 8-cyclopentyl-1,3-dipropylxanthine (DPCPX) (*13*). In the cat and monkey brains, the regional distribution pattern of ^{11}C-MPDX was similar to that of its analog ^{11}C-KF15372 (*13,14*), for which the receptor-specific binding was directly confirmed in the monkey brain (*11*). Furthermore, alteration of ^{11}C-MPDX binding was observed using ex vivo autoradiography in the rat brain treated by monocular enucleation (*12*) and was observed using PET in the cat brain with cerebral ischemic insult (*15*). On the basis of these studies, for the quantitative analysis for ^{11}C-MPDX binding in the human brain, we used Logan plot analysis in the present study because it provides relatively stable results compared with the results of kinetic analysis using a 2- or 3-compartment model.

The DV of ^{11}C-MPDX was relatively smaller in the medial temporal cortex including the hippocampus. In postmortem brain studies, the density of adenosine A_1 receptor binding sites was heterogeneous, and the density was high in the stratum radiatum/pyramidale of CA1 but low in the stratum moleculare of CA1 and the granule cell layer of the dendate gyrus hilus (*20,21*). In ^{11}C-MPDX PET, the DV values in these ROIs were assessed as the means of high and

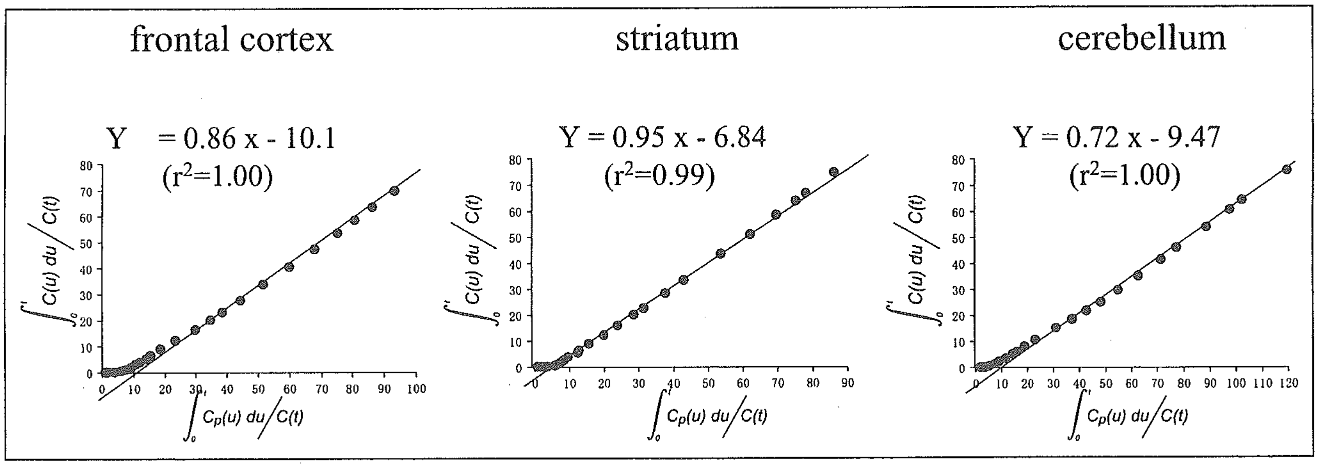

FIGURE 5. Graphical analysis of ^{11}C-MPDX in frontal cortex, striatum, and cerebellum using Logan plot in 1 case. (●), Data used for linear regression analysis. Slopes of fits represent DVs. C = activity in tissue; $Cp(t)$ = activity in plasma; t = elapsed time.

low densities of the binding sites, which resulted in the apparent discrepancy between the in vitro findings and ^{11}C-MPDX PET in the medial temporal cortex. The partial-volume effect based on the spatial resolution may be the other reason why the DV in the medial temporal cortex was relatively small.

We performed successively 2 PET scans with ^{15}O-H$_2$O and ^{11}C-MPDX in each subject to verify the influence from rCBF. As shown in Figure 4 and Table 1, the DV pattern was distinctly different from the rCBF pattern. The DV was large in the striatum and thalamus and small in the cerebellum showing a high rCBF. Together with the finding that the DV pattern was consistent with the in vitro receptor distribution pattern in the described postmortem studies (*20,21*), we concluded that the DV calculated by Logan plot analysis was a stable and sufficient method to estimate the binding of ^{11}C-MPDX to adenosine A$_1$ receptors.

As shown in the time–activity curves of whole blood and plasma (Fig. 2), the radioactivity level in blood was slightly higher than that of plasma. The finding suggests the presence of binding sites or an unknown uptake mechanism for ^{11}C-MPDX in blood cells. With regard to the peripheral metabolism of the tracer, we found that ^{11}C-MPDX was relatively stable in our human subjects compared with the metabolism in experimental animals. The unchanged form of ^{11}C-MPDX in human plasma was 75% of the total radioactivity at 60 min after injection, whereas the corresponding figures were 22%–27% at 30 min in rats (*10*), 6.5% at 60 min in cats (*13*), and 41% at 60 min in monkeys (*15*).

Recently, Bauer et al. also successfully performed imaging of adenosine A$_1$ receptors in the human brain by PET using a similar radioligand, ^{18}F-CPFPX (*16*). They also evaluated the binding of ^{18}F-CPFPX as the DV. The distribution pattern of ^{11}C-MPDX was consistent with that of ^{18}F-CPFPX. However, for the peripheral metabolism, ^{11}C-MPDX was much more stable than ^{18}F-CPFPX. The unchanged form of ^{18}F-CPFPX in the plasma decreased rapidly <25% after 10 min after injection, whereas the percentages of unchanged ^{11}C-MPDX in the plasma remained high during the 60-min PET scan: 89% at 10 min and 75% at 60 min after injection. Although ^{11}C-MPDX (inhibition constant [K_i] = 4.2 nmol/L for the rat forebrain membrane) (*10*) has a slightly lower affinity for A$_1$ receptors than ^{18}F-CPFPX (K_i = 1.26 nmol/L for the cloned human A$_1$ receptors) (*25*), the in vivo stability of ^{11}C-MPDX is the advantage of the continuous input function for the kinetic analysis. On the other hand, ^{18}F-CPFPX has practical advantages: ^{18}F provides a slightly better resolution of the images and its longer half-life of is more suitable to handle in clinical use compared with ^{11}C-labeled tracers.

Coexpression of and functional interactions between adenosine A$_1$ and dopamine D$_1$ receptors in the striatum of rat and rabbit have been reported (*26*). The similarity in distribution of these receptors types suggests that such an interaction might also occur in the human brain. They are important for cholinergic neurotransmission. Adenosine plays an important role in sleep, and adenosine receptor antagonists such as caffeine promote wakefulness and disrupt normal sleep (*4,27*). Studies on the postmortem human brain reported a reduced density of adenosine A$_1$ receptors in the hippocampus of patients with Alzheimer's disease (*28–30*). The anticonvulsant effects of adenosine appear to be mediated primarily by A$_1$ receptors (*31,32*). Carter et al. reported that arousal detected by electroencephalography after caffeine ingestion might be due to increased cholinergic activity (*33*). Angelatou et al. detected a significant increase in adenosine A$_1$ receptor binding in the neocortex obtained from patients with temporal lobe epilepsy (*34*), whereas Glass et al. found that the adenosine A$_1$ receptors were reduced in epileptic temporal cortex in temporal lobes removed from patients with complex partial seizures (*35*). The ^{11}C-MPDX PET is of great interest in establishing the diagnosis of patients with somnipathy, epilepsy, Alzheimer's disease, and other neurologic and psychiatric diseases and understanding the pathogenesis and treatment effect.

CONCLUSION

^{11}C-MPDX was widely but discretely distributed with different concentrations in the brain. The binding of ^{11}C-MPDX was high in the striatum and thalamus, intermediate in the cerebral cortices, and low in the cerebellum. The distribution pattern of ^{11}C-MPDX was consistent with that of adenosine A$_1$ receptors in vitro but discretely different from that of rCBF. The ^{11}C-MPDX PET has the potential for mapping adenosine A$_1$ receptors in the human brain. ^{11}C-MPDX PET is useful for mapping adenosine A$_1$ receptors in the human brain.

REFERENCES

1. Collis MG, Hourani SMO. Adenosine receptor subtypes. *Trends Pharmacol Sci.* 1993;14:360–366.
2. Fredholm BB, Abbracchio MP, Burnstock G, et al. Nomenclature and classification of purinoceptors. *Pharmacol Rev.* 1994;46:143–156.
3. Haas HL, Selbach O. Functions of neuronal adenosine receptors. *Naunyn Schmiedebergs Arch Pharmacol.* 2000;362:375–381.
4. Dunwiddie TV, Masino SA. The role and regulation of adenosine in the central nervous system. *Annu Rev Neurosci.* 2001;24:31–55.
5. von Lubitz DK. Adenosine in the treatment of stroke: yes, maybe, or absolutely not? *Expert Opin Investig Drugs.* 2001;10:619–632.
6. Yacoubi ME, Costentin J, Vaugeois JM. Adenosine A$_{2A}$ receptors and depression. *Neurology.* 2003;61:S82–S87.
7. Suzuki F, Ishiwata K. Selective adenosine antagonists for mapping central nervous system adenosine receptors with positron emission tomography: carbon-11 labeled KF15372 (A$_1$) and KF17837 (A$_{2A}$). *Drug Develop Res.* 1998;45:312–323.
8. Ishiwata K, Shimada J, Ishii K, Suzuki F. Assessment of the adenosine A$_{2A}$ receptors with PET as a new diagnostic tool for neurological disorders. *Drugs Fut.* 2002;27:569–576.
9. Fukumitsu N, Ishii K, Kimura Y, et al. Imaging of adenosine A$_1$ receptors in the human brain by positron emission tomography with [^{11}C]MPDX. *Ann Nucl Med.* 2003;17:511–515.
10. Noguchi J, Ishiwata K, Furuta R, et al. Evaluation of carbon-11 labeled KF15372 and its ethyl and methyl derivatives as a potential CNS adenosine A$_1$ receptor ligand. *Nucl Med Biol.* 1997;24:53–59.
11. Wakabayashi S, Nariai T, Ishiwata, et al. A PET study of adenosine A1 receptor in anesthetized monkey brain. *Nucl Med Biol.* 2000;27:401–406.
12. Kiyosawa M, Ishiwata K, Noguchi J, et al. Neuroreceptor bindings and synaptic

activity in visual system of monocularly enucleated rat. *Jpn J Ophthalmol.* 2001;45:264–269.

13. Shimada Y, Ishiwata K, Kiyosawa M, et al. Mapping adenosine A$_1$ receptors in the cat brain by positron emission tomography with [^{11}C]MPDX. *Nucl Med Biol.* 2002;29:29–37.
14. Ishiwata K, Nariai T, Kimura Y, et al. Preclinical studies on [^{11}C]MPDX for mapping adenosine A$_1$ receptors by positron emission tomography. *Ann Nucl Med.* 2002;16:377–382.
15. Nariai T, Shimada Y, Ishiwata K, et al. PET imaging of adenosine A$_1$ receptors with ^{11}C-MPDX as an indicator of severe cerebral ischemic insult. *J Nucl Med.* 2003;44:1839–1844.
16. Bauer A, Holschbach MH, Meyer PT, et al. In vivo imaging of adenosine A$_1$ receptors in the human brain with [^{18}F]CPFPX and positron emission tomography. *Neuroimage.* 2003;19:1760–1769.
17. Ardekani BA, Braun M, Hutton BF, Kanno I, Iida H. A fully automatic multimodality image registration algorithm. *J Comput Assist Tomogr.* 1995;19:615–623.
18. Herscovitch P, Markham J, Raichle ME. Brain blood flow measured with intravenous H$_2$^{15}O. I. Theory and error analysis. *J Nucl Med.* 1983;24:782–789.
19. Logan J, Fowler JS, Volkow ND, et al. Graphical analysis of reversible radioligand binding from time-activity measurements applied to [N-^{11}C-methyl]-(-)-cocaine PET studies in human subjects. *J Cereb Blood Flow Metab.* 1990;10: 740–747.
20. Svenningsson P, Hall H, Sedvall G, Fredholm BB. Distribution of adenosine receptors in the postmortem human brain: an extended autoradiographic study. *Synapse.* 1997;27:322–335.
21. Fastbom J, Pazos A, Probst A, Palacios JM. Adenosine A$_1$ receptors in the human brain: a quantitative autoradiographic study. *Neuroscience.* 1987;22:827–839.
22. Lewis ME, Patel J, Moon ES, Marangos PJ. Autoradiographic visualization of rat brain adenosine receptors using N^6-cyclohexyl[^{3}H]adenosine. *Eur J Pharmacol.* 1981;73:109–110.
23. Goodman RR, Snyder SH. Autoradiographic localization of adenosine receptors in rat brain using [^{3}H]cyclohexyladenosine. *J Neurosci.* 1982;2:1230–1241.
24. Fastbom J, Pazos A, Palacios JM. The distribution of adenosine A1 receptors and 5′-nucleotidase in the brain of some commonly used experimental animals. *Neuroscience.* 1987;22:813–826.
25. Holschbach MH, Olsson RA, Bier D, et al. Synthesis and evaluation of non-carrier-added 8-cyclopentyl-3-(3-[^{18}F]fluoropropyl)-1-propylxanthine ([^{18}F]CPFPX): a potent and selective A$_1$-adenosine receptor antagonist for in vivo imaging. *J Med Chem.* 2002;45:5150–5156.
26. Ferre S, O'Connor WT, Svenningson P, et al. Dopamine D$_1$ receptor-mediated facilitation of GABAergic neurotransmission in the rat strioentopeduncular pathway and its modulation by adenosine A$_1$ receptor-mediated mechanisms. *Eur J Neurosci.* 1996;8:1545–1553.
27. Radulovadei M. Role of adenosine in sleep in rats. *Rev Clin Basic Pharmacol.* 1985;5:327–339.
28. Jansen K, Faull RLM, Dragunow M, Synek BJL. Alzheimer's disease: changes in hippocampal *N*-methyl-D-aspartate, quisqualate, neurotensin, adenosine, benzodiazepine, serotonin and opioid receptors—an autoradiographic study. *Neuroscience.* 1990;39:613–627.
29. Ulas J, Brunner LC, Nguyen L, Cotman CW. Reduced density of adenosine A1 receptors and preserved coupling of adenosine A1 receptors to G proteins in Alzheimer hippocampus: a quantitative autoradiographic study. *Neuroscience.* 1993;52:843–854.
30. Deckert J, Abel F, Kunig G, et al. Loss of human hippocampal adenosine A1 receptors in dementia: evidence for lack of specificity. *Neurosci Lett.* 1998;244: 1–4.
31. Murray TF, Franklin PH, Zhang G, Tripp E. A$_1$ adenosine receptors express seizure-suppressant activity in the rat prepiriform cortex. *Epilepsy Res Suppl.* 1992;8:255–261.
32. Zhang G, Franklin PH, Murray TF. Activation of adenosine A1 receptors underlies anticonvulsant effect of CGS21680. *Eur J Pharmacol.* 1994;255: 239–243.
33. Carter AJ, O'Connor WT, Carter MJ, Ungerstedt U. Caffeine enhances acetylcholine release in the hippocampus in vivo by a selective interaction with adenosine A1 receptors. *J Pharmacol Exp Ther.* 1995;273:637–642.
34. Angelatou F, Pagonopoulou O, Maraziotis T, et al. Upregulation of A1 adenosine receptors in human temporal lobe epilepsy: a quantitative autoradiographic study. *Neurosci Lett.* 1993;163:11–14.
35. Glass M, Faull RL, Bullock JY, et al. Loss of A1 adenosine receptors in human temporal lobe epilepsy. *Brain Res.* 1996;710:56–68.

13. Alzheimer病

石井賢二

わが国は未曾有の高齢化社会を迎えようとしており，認知症の対策は緊急の課題となっている．Alzheimer病に対する従来の治療戦略は，発症後に対症的治療を行うのみであったが，病態の分子レベルでの解明が現在急ピッチで進められており，できるだけ早期にあるいは発症前の段階で診断し，疾患の発症や進展を食い止める方向へと近い将来大きくシフトすることが予想される．FDG-PETはAlzheimer病の早期診断，鑑別診断に最も感度，特異性の高い検査であり，脳血流シンチよりも感度が高い．現在日本ではFDG-PETによるAlzheimer病の診断に保険適応は認められていないが，アメリカでは昨年Alzheimer病と前頭側頭型痴呆症（FTD）の鑑別診断に保険適応が認められた．早期診断についても充分なエビデンスが揃えば適応が認められる方向である．わが国では，癌診断によるPET機器の普及がすでに先行しているので，今後Alzheimer病早期診断に対するニーズが高まり，保険適応への道が開かれればPETによる診断も急速に普及していくものと考えられる．本稿では，PETによるAlzheimer病診断の現状と展望について述べる．

変性マーカーとしての糖代謝測定の意義

脳は，その神経活動のエネルギー源をもっぱらブドウ糖の酸化的リン酸化に依存している．FDG-PETによる局所脳ブドウ糖代謝画像は局所の神経活動をよく反映している．Alzheimer病はシナプス機能の低下が神経細胞脱落に先行するので，形態的な萎縮が生じるよりも前に，神経活動の低下を局所糖代謝の低下としてFDG-PETで感度よくとらえることができる．また，疾患ごとに脳機能低下を生じやすい場所に特徴があるので，鑑別診断にも有用である．

Alzheimer病のPET画像の特徴

Alzheimer病は，病理学的には側頭葉の内嗅野の変化が最も早期にはじまるといわれているが，機能画像でとらえることのできる最も早期の変化は後部帯状回や前楔部の代謝低下である．その後，糖代謝低下は頭頂葉，側頭葉の外側部におよび，進行すると側頭葉の内側や前頭葉の代謝も低下してくる．一次運動感覚野や後頭葉は進行しても代謝の低下は比較的少ない．我々の経験では，CDR 0.5，MMSE 24点以上のいわゆるMCI相当の患者においても，FDG-PETではすでに明確な側頭頭頂葉の低下を示す典型的なpatternを呈していることが多く，このことからみると，FDG-PETを使えば，かなり早期の段階で診断が可能であると考えられる．

図1は，各病期のAlzheimer病におけるFDG-PET画像の平均的な特徴を示している．しかし，実際には個々の症例でみると，代謝低下のpatternはきわめて多彩であり（図2），視覚的読影のみで診断することは，特に早期の症例では必ずしも容易ではない．そこで，読影者に依存しない客観的な画像の判定方法として，統計画像法が広く用いられるようになってきた．症例の画像を標準脳に変形し，画素ごとに正常群と比較して，統計学的に有意な代謝低下のある部位を検出する技法で，3DSSPやSPMが用いられている．特に早期の軽微な代謝低下を検出する感度に優れている．図3は，自覚的な物忘れで受診した早期Alzheimer病例のSPMによる統計画像である．

Alzheimer病と鑑別の必要な変性型痴呆疾患

日常臨床においてAlzheimer病と鑑別が必要な変性型痴呆症のFDG-PET画像の特徴について述べる．これらの特徴は，脳血流SPECTともほぼ

いしい けんじ／東京都老人総合研究所ポジトロン医学研究施設診療所長

共通しており，SPECTの読影にも適用できる．

●前頭側頭型痴呆（FTD）

非Alzheimer病型痴呆症の中で脳の前方部を中心に病巣を認める疾患をよび，従来から知られたPick病のほか，脳萎縮を伴わない前頭葉変性型痴呆症，痴呆を伴う運動ニューロン疾患が含まれ，広義には言語機能の障害を特徴とする進行性失語症や意味記憶の障害を特徴とするsemantic dementiaもこれに含まれる．したがって，FTDとは症候群であり，単一の疾患でないことに注意しなければならない．FDG-PETでは初期から脳前方部の機能が低下することを反映してAlzheimer病とは対照的なパターンを呈する（図4）．

●Lewy小体型痴呆症（DLB）

Parkinson病脳で変性脱落する黒質線条体ドパミン産生ニューロンに認められるLewy小体が大脳皮質にも広汎に出現する疾患で，Parkinson病が先行し痴呆が加わるタイプとParkinson症状に対して痴呆症状がほぼ同時あるいは先行するものに分類するのが一般的であるが，疾患としては一連のスペクトラムに属するものと考えられる．FDG-PETの特徴はAlzheimer病と同様に，後部帯状回，前楔部，側頭頭頂葉皮質に代謝低下がみられるので，機能画像による診断の際はAlzheimer病との鑑別が問題となる．DLBではAlzheimer病では比較的よく保たれる後頭葉皮質の代謝低下が認められることが特徴であり，また，線条体や海馬の代謝がAlzheimer病に比べて相対的に高いことも鑑別のポイントとなる（図5）．近年，donepezil hydrochlorideを投与されたAlzheimer病患者が増えているが，donepezil hydrochlorideの服用は線条体の代謝をやや亢進させる作用があるので，DLBとの異同を鑑別する際には注意を要する．

●進行性核上性麻痺（PSP）

Parkinson症状，特に立位バランス障害に加え，垂直眼球運動障害，仮性球麻痺などとともに痴呆症状を呈する疾患である．臨床症状は多彩で，痴呆症状が前面に発症することがあり，他の痴呆性疾患との鑑別が必要となるが，運動障害や嚥下構音障害が比較的早く進行するので介護上困難の多い疾患である．FDG-PETでは前帯状回や前頭弁蓋部の代謝低下が特徴であるほか，中脳の代謝低下が早期からみられることが特徴である（図6）．

●皮質基底核変性症（CBD）

左右差の比較的はっきりした運動障害，特にalien handとよばれるようなジストニア肢位または運動を特徴とするが，皮質の巣症状で発症することもある．FDG-PETの所見は，皮質の一部と線条体，視床の代謝低下が一側に強く認められることである．特に中心前回に強い萎縮を伴う代謝低下が認められることが多い（図7）．左右差は初期に強く，進行とともにめだたなくなる．

●嗜銀顆粒性痴呆（DAG）

病理学的にはグレインとよばれる嗜銀性顆粒が側頭葉の内側部を中心に出現する．臨床疾患概念としてはまだ確立されていないが，連続剖検における検討ではAlzheimer病に匹敵する頻度があるという報告もある．高齢者に多く，健忘症状が主体で進行の比較的緩徐な痴呆症を呈する．Alzheimer病と診断されたり，高齢のために生前は痴呆として認識されていない症例もある．今後，臨床診断基準の確立が必要な疾患であり，軽度認知障害（MCI）の中に含まれ，Alzheimer病と鑑別が必要な疾患として考慮する必要がある．嗜銀顆粒性痴呆と考えられる症例のFDG-PETの特徴は側頭葉内側部に比較的限局した糖代謝の低下で，側頭葉外側部や頭頂葉の代謝は相対的によく保たれる（図8）．

今後の展望について

これまでAlzheimer病の診断におけるFDG-PETの役割について述べてきたが，今後の方向性についていくつか話題を紹介したい．

Alzheimer病の脳機能改善，あるいは病態メカニズムの進展を食い止めるための治療法の開発が精力的に進められている．従来の薬剤の治験は主として行動学的な指標に基づいていたが，FDG-PETで脳代謝をモニターすることにより，薬剤の効果をより直接的・客観的に検証することが期待できる．薬剤に限らず，音楽療法や絵画療法など行動学的な治療法も含め，さまざまな介入的治療・予防法の効果を検証する手段として使うことができると考えられる．donepezil hydrochlorideによる効果をみた例を示す（図9）．また，ピッツバーグ大などにより，Alzheimer病で老人斑を形成するβアミロイドを標識するPET製剤が開発されている．この検査法は感度が高いので，発症前診断や，根本的な治療法のモニターに利用ができると期待されている．

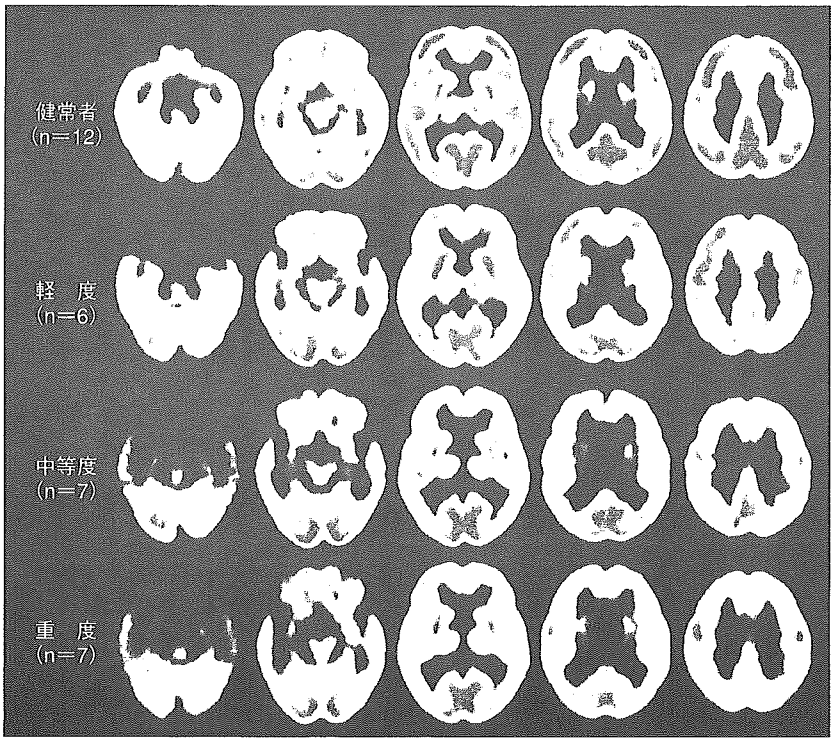

図1　Alzheimer病の進行に伴うFDG-PET画像の平均的変化

代謝低下は後部帯状回，前楔部，にはじまり，頭頂葉・側頭葉外側，側頭葉内側，前頭葉に及ぶ．後頭葉や一次運動感覚野は比較的よく保たれる．

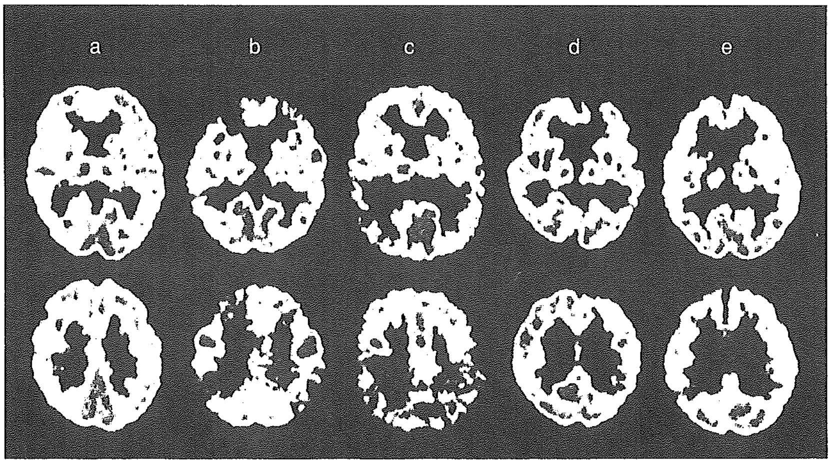

図2　Alzheimer病のFDG-PET画像の個人差

5例（aからe）の画像を示す．左右差のめだつ症例や，前頭葉の代謝低下が初期からめだつ症例など個々の症例の画像は多彩である．

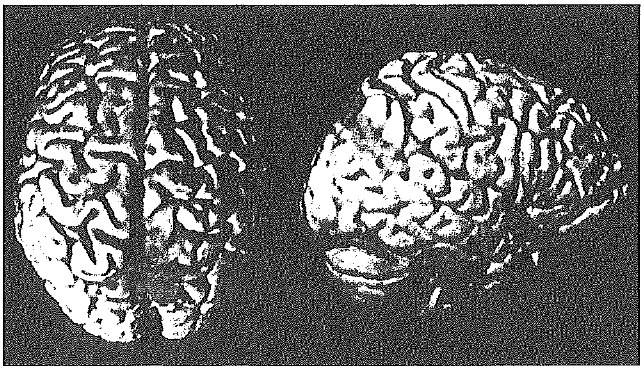

図3　統計画像（SPM）による早期Alzheimer病の診断

健常群と比較して，有意な代謝低下部位を脳表画像に赤く表示．症例は76歳男性，自覚的もの忘れで受診したが生活に障害はない．MMSE 28点，CDR 0.5であった．後部帯状回の代謝低下が検出されている．

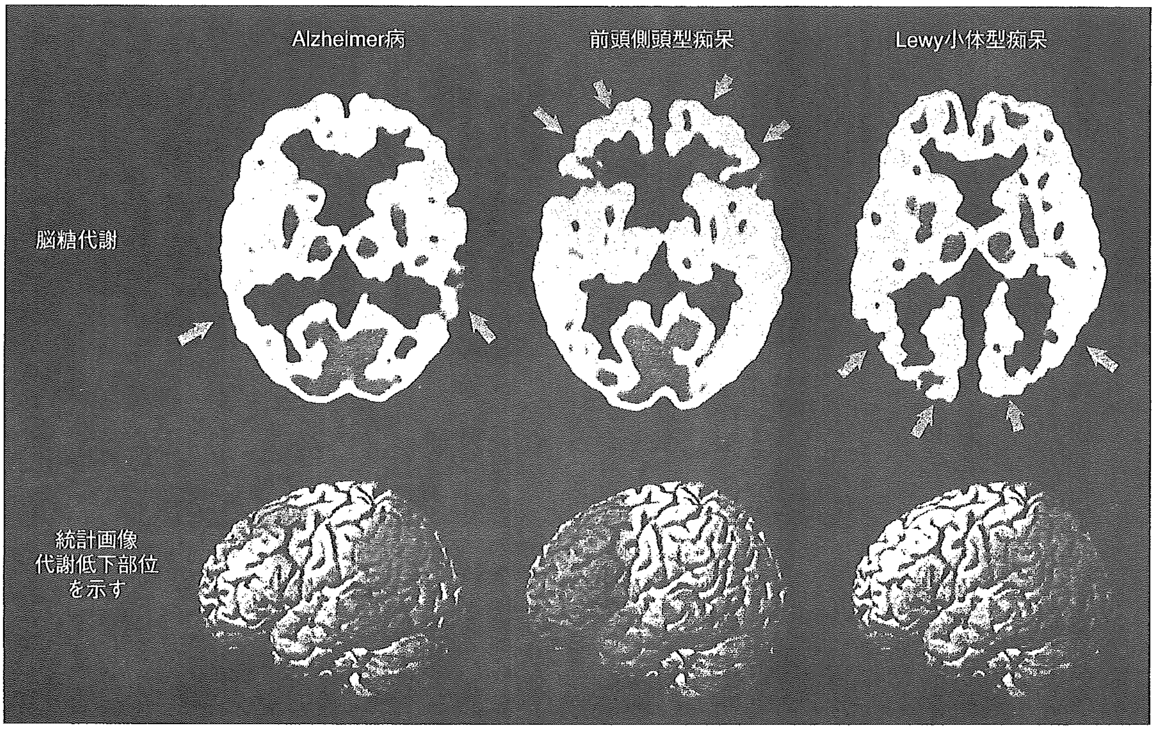

図4　代表的痴呆疾患の症例のFDG-PET画像
左から，Alzheimer病，前頭側頭型痴呆症，Lewy小体型痴呆症のFDG-PET画像と統計画像を示す．それぞれの疾患に特徴的な代謝低下パターンが認められる．

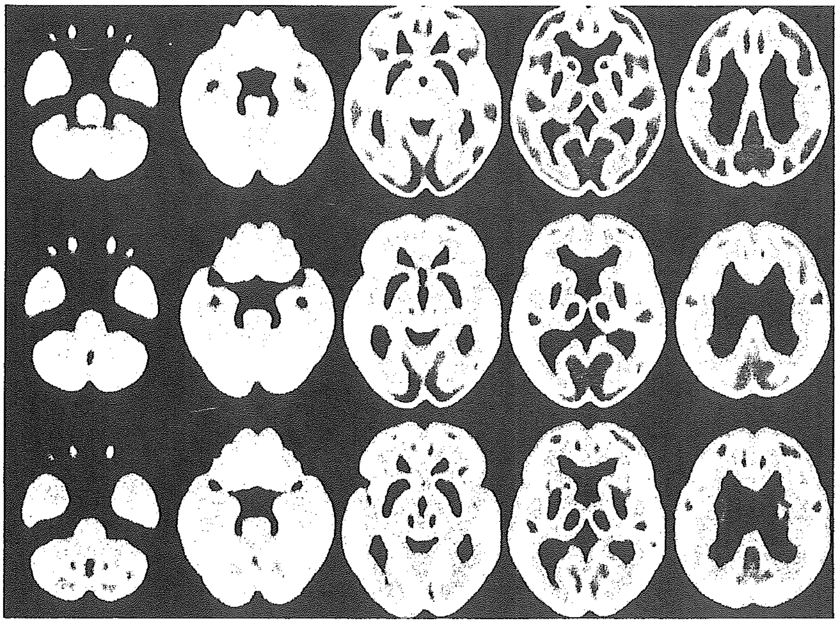

図5　Alzheimer病とLewy小体型痴呆症のPET画像の比較
上段: 健常者（51例），中段: Alzheimer病(52例)，下段: Lewy小体型痴呆症(18例）の平均画像を示す．両疾患で皮質代謝低下のパターンはよく似ているが後頭葉や海馬，線条体の代謝低下に違いがみられる．

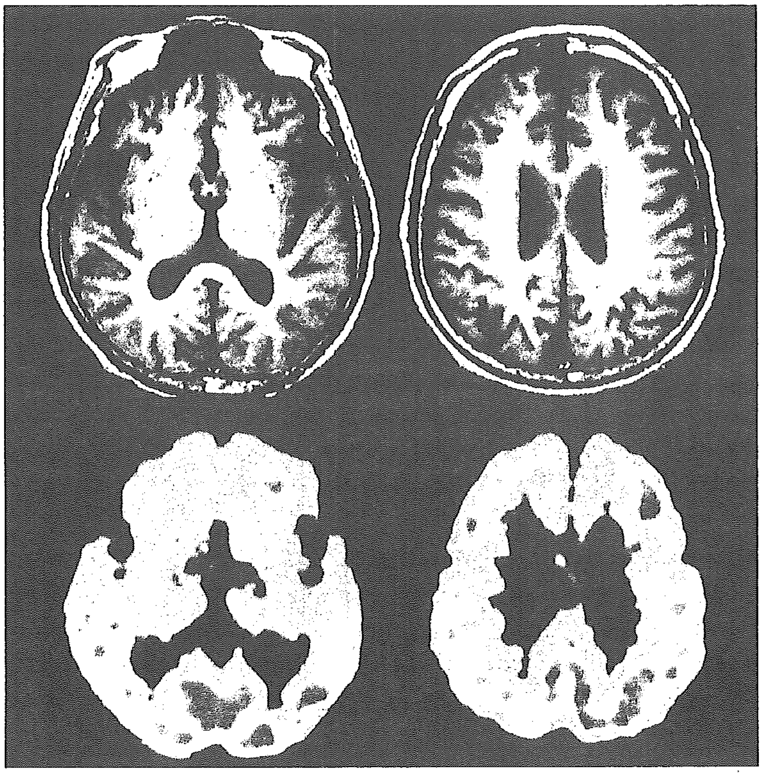

図6　進行性核上性麻痺のPET画像

69歳，男性．易転倒傾向で発症し，構音障害，記銘力低下が加わった．前頭葉内側部，前頭弁蓋部の代謝低下を認める．

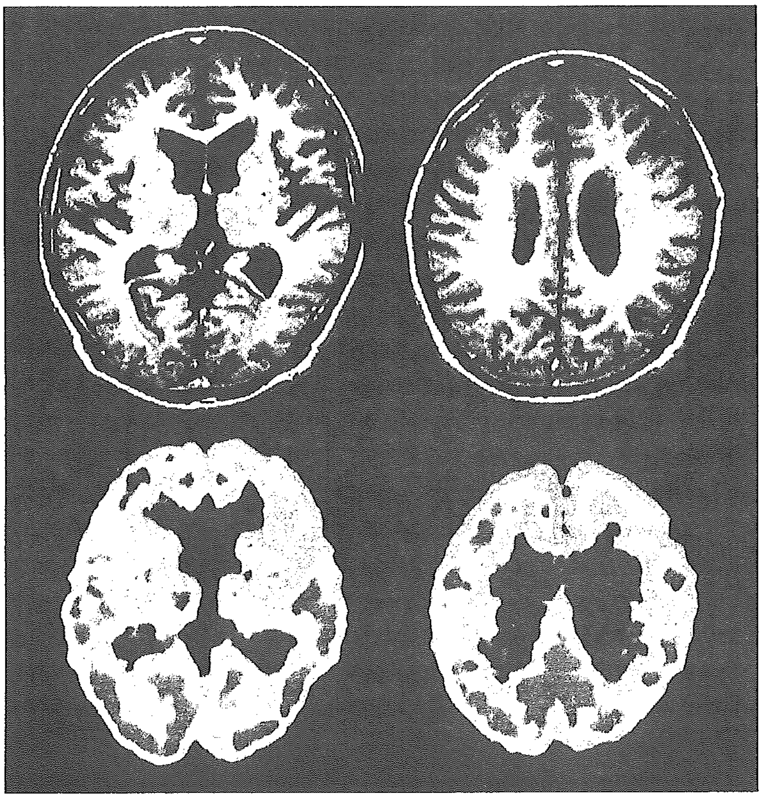

図7　皮質基底核変性症のPET画像

72歳，男性．右手の巧緻運動障害，ジストニア肢位で発症．中心前回を含めた左前頭葉，左被殻，左視床の代謝低下を認め，左右差がめだつ．

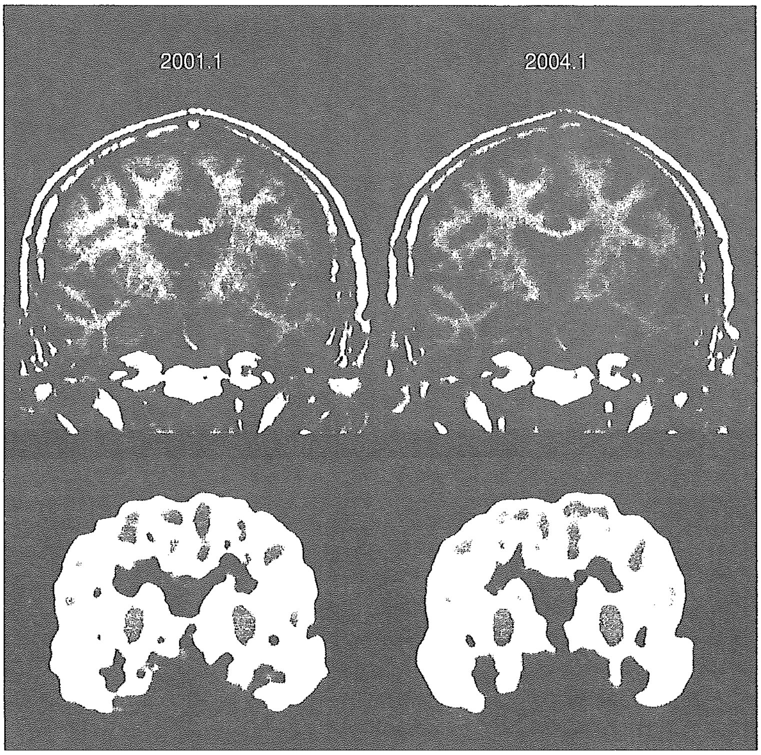

図8　嗜銀顆粒性痴呆を疑われる症例のPET画像

82歳，女性．病識の乏しい健忘症状で受診．進行は緩徐で身辺のことはできる．側頭葉内側の代謝低下が進行するが，他の部位は比較的よく保たれる．

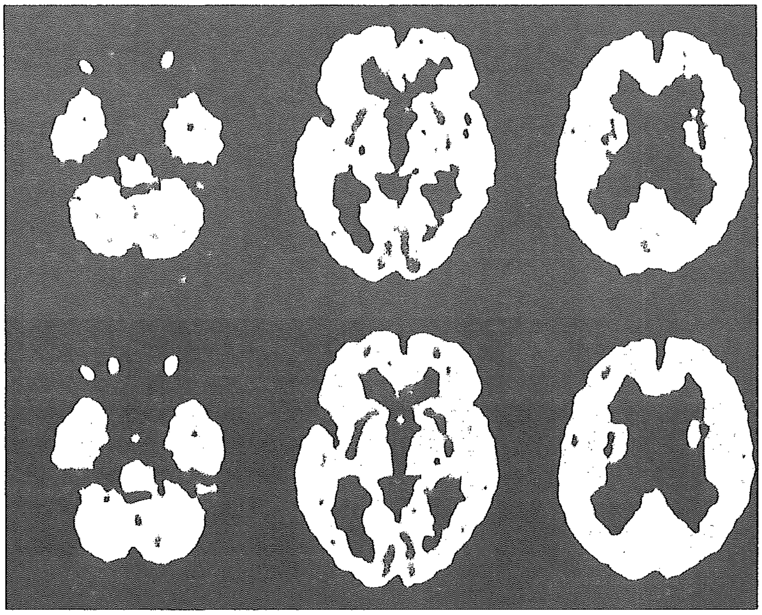

図9　donepezil hydrochloride 治療の効果

59歳，男性．上段: 治療開始前，下段: 投与開始から5カ月後．両側前頭葉の糖代謝が改善している．しかし右頭頂葉の代謝低下は進行しており，脳全体の機能が改善されるわけではない．

文　献

1) Knopman DS, et al. Practice parameter: Diagnosis of dementia (an evidence-based review). Neurology. 2001; 56: 1143–53.
2) Silverman DH, et al. Positron emission tomography in evaluation of dementia. JAMA. 2001; 286: 2120–7.
3) Neuroimaging Work Group of Alzheimer's Association. The use of MRI and PET for clinical diagnosis of dementia and investigation of cognitive impairement. A consensus report. (http://www.alz.org/Research/papers.asp)

ORIGINAL RESEARCH

Optic Nerve Hyperintensity on T2-Weighted Images among Patients with Pituitary Macroadenoma: Correlation with Visual Impairment

A.M. Tokumaru
I. Sakata
H. Terada
S. Kosuda
H. Nawashiro
M. Yoshii

PURPOSE: Visual acuity (VA) disturbance other than field defect is important in evaluating patients with pituitary macroadenoma. The purpose of this study was to evaluate MR imaging appearances of optic nerves in patients with pituitary macroadenoma and to ascertain whether visual impairment was correlated with abnormality in optic nerve signal intensity.

PATIENTS AND METHODS: Twenty-seven patients with pituitary macroadenoma were examined. Optic nerves were evaluated on T2-weighted images and correlations of signal intensity abnormality with VA disturbance, visual field disturbance, degree of optic chiasm compression, pathologic findings of surgical specimen, and disease duration were statistically analyzed. Correlations between recovery of VA after treatment and the above-mentioned factors were also determined.

RESULTS: Coronal T2-weighted images demonstrated unilateral optic nerve hyperintensity lesions in 9 patients. Bilateral signal intensity abnormality of the optic nerve was seen in 5 patients. Signal intensity abnormality of the optic nerve was seen at the site of compression and in the ventral side of the tumor. These patients did not demonstrate signal intensity abnormality posterior to the tumor. Presence of such signal intensity abnormalities was correlated with the degree of optic chiasmal compression and with VA disturbance. Recovery of VA after treatment was correlated with disease duration.

CONCLUSION: Hyperintensity of the optic nerves ventral to the pituitary macroadenoma was associated with VA impairment. Recovery of VA after treatment was correlated with disease duration. MR imaging of the optic nerves can provide valuable information for management of pituitary macroadenoma.

In some patients with pituitary macroadenoma, visual acuity (VA) diminishes despite the existence of no field defect other than bitemporal hemianopia. This clinical information is very important in patient management; however, no published reports have analyzed the relationship between VA disturbance and MR imaging findings of the optic nerves of the patients with the pituitary macroadenoma. In this study, the authors used T2-weighted MR imaging to investigate signal intensity abnormality of the optic nerves and statistically analyzed the relationship between this and factors including the degree of optic chiasm compression, disease duration, degree of VA disturbance, and tumor histopathology.

Hyperintensity of the optic nerves was frequently detected among patients with diminished VA. Among those with long disease duration and prolonged signal intensity abnormality, improvements in VA disturbance tended to be poor, which suggests the possibility of degeneration of optic nerves caused not only by compression-induced edema, but also by compression of the arteries, veins, and capillary networks in the optic chiasm.

Patients and Methods

We reviewed pre- and postoperative MR images from 27 consecutive patients with pituitary macroadenoma, 24 of whom were treated surgically at the National Defense Medical College between April 1999 and November 2003. All MR examinations were performed by using a 1.5T system. We used fast spin-echo sequences for T2-weighted (3500/110/2) and T1-weighted (500/15/1) images. Three-millimeter-thick sections were obtained in the coronal and sagittal planes with a 256 × 512 acquisition matrix. All images were blindly reviewed by 2 radiologists, focusing on the presence of abnormal signal intensity in the optic nerves ventral to the tumor, at the site of compression, and dorsal to the tumor. We also classified degree of optic chiasm compression into 3 grades as follows: (−) no compression; (+) compression of less than half of the optic chiasm; and (++) compression with severe thinning. Signal intensity abnormality of the optic nerve was defined as abnormality involving not only the area around the optic nerve, but also the septum (+). In patients with (+) or (++) compression, we also evaluated the location of the tumor in relation to the optic nerve and optic chiasm. Cephalocaudal diameter of each tumor was also measured

Visual signs (visual field defect and VA) were evaluated by an ophthalmologist. Twenty-four patients underwent surgical procedures, and histologic confirmation of the diagnosis was obtained in each case.

A Mann-Whitney *U* test was used for statistical analysis of the relationships between signal intensity abnormality and tumor size, degree of chiasm compression, histology, VA disturbance, and disease duration. Correlations between recovery of VA after treatment and the above-mentioned factors were also ascertained.

Results

Patient clinical data are summarized in Table 1. The results are shown in Figs 1–4.

Received August 1, 2004; accepted after revision July 23, 2005.

From the Department of Radiology (A.M.T.), Tokyo Metropolitan Geriatric Hospital, Tokyo Japan; Departments of Radiology (I.S., S.K.) and Neurosurgery (H.N.), National Defense Medical College, Saitama Japan; Department of Ophthalmology (M.Y.), National Rehabilitation Center for Persons with Disabilities, Saitama Japan; and The 2nd Department of Radiology (H.T.), Toho University School of Medicine, Tokyo Japan.

Address correspondence to Aya M.Tokumaru, Department of Radiology, Tokyo Metropolitan Geriatric Hospital, 35-2 Sakae-Cho, Itabashi-Ku, Tokyo, Japan 173-0015.

Optic tract hyperintensity on T2-weighted images among patients with pituitary macroadenoma: correlation with visual impairment

Patient No./ Age (y)/Sex	Duration	Size (mm)	OC	AS	VAD	VFD	Pathology	IAT
1/36/M	2 mo	18	−	−	−	+		
2/61/M	9 y	23.7	+	−	+ (rt 0.7, lt blind)	+	PA	−
3/42/F	16 mo	26.5	++	+	+ (rt 0.02, lt 1.5)	+	PA (corticotro)	−
4/38/F	10 mo	14	−	−	−	+		
5/40/M	6 mo	35	++	+	+ (rt 0.07, lt 0.05)	+	PA (null)	−
6/55/F	4 y	46	++	+	+ (rt 0.06, lt 0.06)	+	PA (chromophobe)	−
7/65/F	2 mo	13	−	−	−	+	PA (null)	
8/74/M	18 mo	16.4	+	+	+ (rt 0.7, lt 0.4)	+	PA (null)	−
9/54/F	3 mo	27	+	+	+ (rt 0.06, lt 0.1)	+	PA (nonfunctioning)	+ (rt 1.2, lt 0.8)
10/65/M	2 mo	13	−	+	+ (rt light sense)	+	Pituitary carcinoma	−
11/59/F	14 mo	35	++	+	+ (rt 0.3, lt 0.9)	+	PA (null)	−
12/55/M	3 mo	22	++	+	+ (rt 0.5, lt 0.1)	+	PA	+ (rt 1.0, lt 1.0)
13/41/F	19 mo	25	++	+	+ (hand sense)	+	PA (null)	−
14/37/F	3 mo	16	−	−	−	+		
15/70/F	6 mo	18	+	+	+ (rt 0.1, lt blind)	−		
16/27/M	6 mo	15	−	+	+ (finger sense)	+	PA (chromophobe)	+ (rt 0.7, lt 0.9)
17/58/M	26 mo	24	++	+	+ (rt 1.5, lt 0.4)	−	PA (null)	−
18/21/F	8 mo	30	+	−	−	+	PA (GH)	−
19/50/F	10 y	51	++	+	+ (rt 0.03, lt 0.1)	+	PA(FSH-LH)	−
20/74/F	1.5 mo	18	−	+	+ (lt light sense)	−	PA (prolactinoma)	+ (rt 0.8, lt 0.4)
21/66/F	2 mo	15	−	−	−	−	PA (null)	
22/63/M	2 mo	23.7	++	+	+ (rt 0.1, lt 0.7)	+	PA (chromophobe)	+ (rt 0.7, lt 0.8)
23/54/F	3 mo	13	−	−	−	−	PA	
24/56/F	3 mo	20	−	−	−	−	PA	
25/45/M	2 mo	16	−	−	−	+	PA (chromophobe)	
26/36/M	2 mo	12.2	−	−	−	−		
27/50/M	3 mo	16	++	+	+ (rt 0.9, lt 0.3)	+	PA (GH)	+ (rt 0.9, lt 0.7)

Note.—OC indicates optic chiasm compression; AS, abnormal signal in optic nerve; VAD, visual acuity disturbance; VFD, visual field disturbance; IAT, improvement of visual acuity after treatment; PA, pituitary adenoma; FSH-LH, follicle stimulating hormone-luteinizing hormone; GH, growth hormone.

Coronal T2-weighted images demonstrated unilateral optic nerve hyperintensity lesions in 9 patients. Bilateral signal intensity abnormality of the optic nerve was seen in 5 patients. Signal intensity abnormality of optic nerve was seen at the compression site and at the ventral side of the tumor. No patients demonstrated signal intensity abnormality posterior to the tumor.

Signal intensity normalized in 9 of 21 patients after surgery or other treatment.

Presence of optic nerve hyperintensity lesions was correlated to the degree of optic chiasm compression and to the presence of diminished VA ($P < .01$). In all patients with (++) optic chiasm compression, the optic nerve was compressed beyond 1 cm anterior and posterior to the optic chiasm, and tumor location exhibited no significant correlation to the presence or absence of optic nerve signal intensity abnormality; however, no correlation between hyperintensity and tumor size was demonstrated in this study. Other than in patients with a tumor size <2 cm, the results suggested the need to consider type II error. Hence, the relationship to tumor size might be clarified by studying greater numbers of patients.

After surgery and other forms of treatment, size of the tumor diminished and compression of the optic chiasm resolved. Of patients with improved VA, signal intensity abnormality improved in 4 patients but persisted in 5 cases (Fig. 5). Atrophy of optic nerves was seen on MR imaging in 3 patients in whom VA abnormalities persisted on ophthalmologic examination (Fig. 6). In one case with improved VA, although the degree of compression to the optic chiasm was mild, steroids were administered from an early stage as a result of signal intensity abnormality in optic nerves on MR imaging and papillary edema, leading to an improvement in VA. Degree of improvement in VA was significantly correlated with disease duration but not with any other factors in this study.

Discussion

The literature contains several reports concerning edema-like change along the optic pathway in association with suprasellar tumors such as craniopharyngioma, pituitary adenoma, and meningioma.[1-2] Hyperintensity in the optic nerve ventral to pituitary macroadenoma, however, has not been reported. As far as the management of pituitary macroadenoma is concerned, VA disturbance is an important factor, and, as a result, related diagnostic imaging findings are also of consequence.[7] In the present study, the relationship between optic nerve signal intensity abnormality, degree of optic chiasm compression, and the presence of VA disturbance were statistically analyzed. The results suggested that prolonged compression caused signal intensity abnormality of the optic nerve and VA disturbance. Consequently, decompression should be performed promptly in patients demonstrating compression of the optic chiasm or signal intensity abnormality of the optic nerve.

Signal intensity abnormality persists after decompression, can lead to atrophy, and is associated with a high frequency of VA disturbance and thus appears to represent changes that extend beyond edema. The mechanism by which pituitary macroadenoma appears to damage the optic nerve and impair VA is unclear. VA disturbance, however, cannot be explained

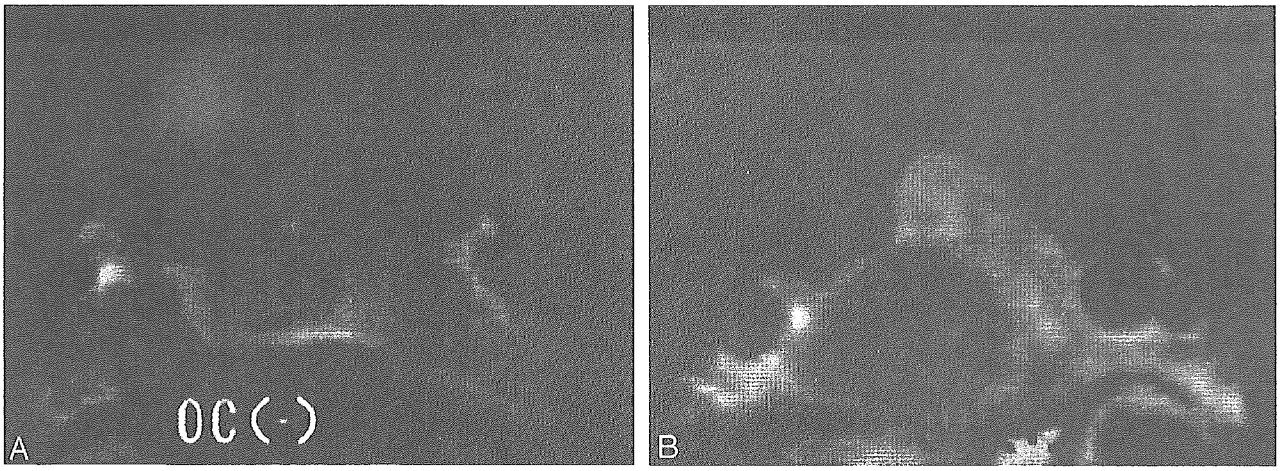

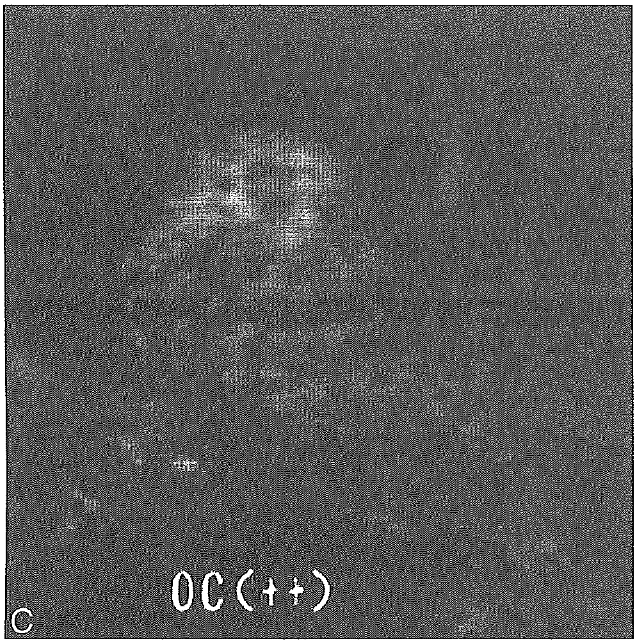

Fig 1. Degree of optic chiasmal compression. *A*, No compression to optic chiasma (−). B, Compression of less than half of the optic chiasm (+). *C*, Compression with marked thinning (++).

solely in terms of mechanical damage due to compression. Because the axons for the entire superior visual field course through the inferior aspect of the optic nerves and chiasm, compression of these structures from below would be expected to produce a defect in the entire upper field. Such defects, however, are extremely rare.[3] As reported by Hoyt, however, compression disrupts the arterial supply, and long-term compression of the arteries, veins, and capillary networks in the optic chiasm leads to stagnant anoxia, thus resulting in a characteristic bitemporal visual field defect.[4] Signal intensity abnormality in the optic nerves was considered to represent damage by compression and stagnant anoxia at the optic chi-

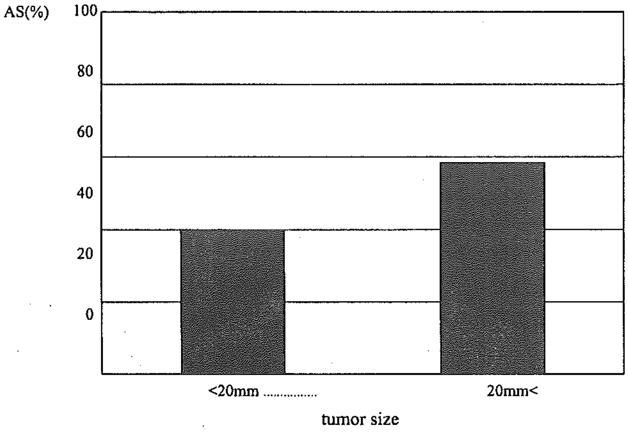

Fig 2. Correlation between abnormal signal intensity of optic nerve and tumor size.

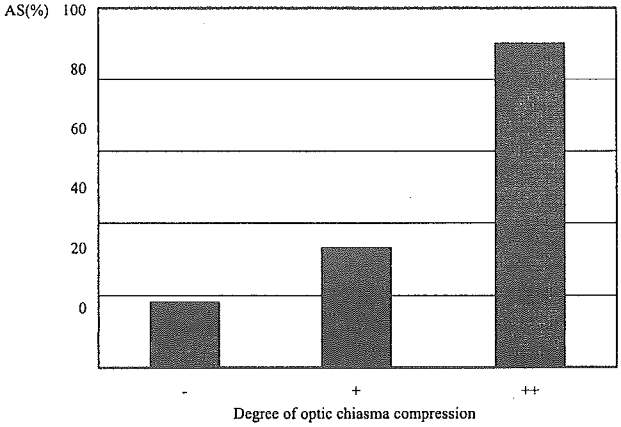

Fig 3. Correlation between abnormal signal intensity of optic nerve and optic chiasm compression.

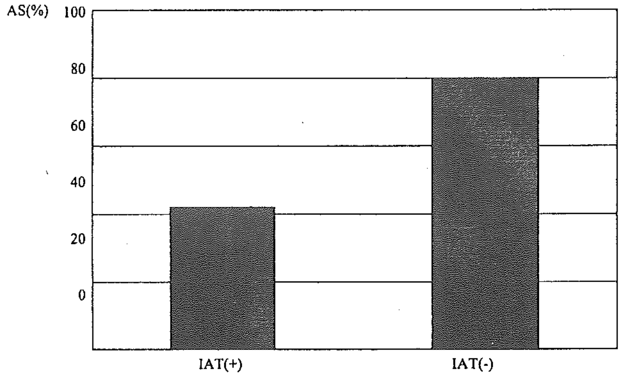

Fig 4. Correlation between abnormal signal intensity of optic nerve and improvement after treatment of VA.

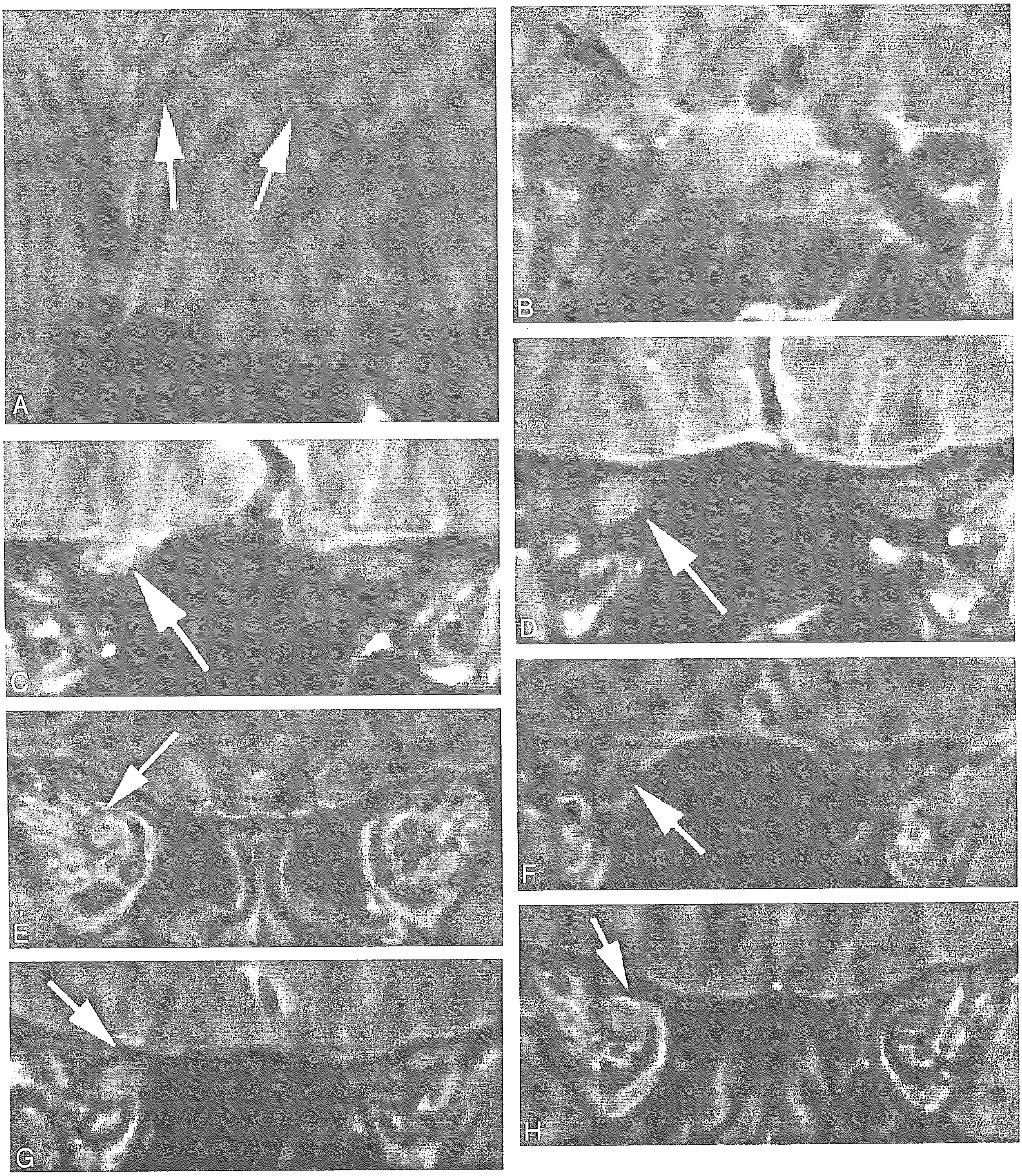

Fig 5. Case 3, a 42-year-old woman whose disease duration was 6 months. Right VA disturbance was recognized (right VA = 0.02; left VA = 1.5). *A*, Pituitary macroadenoma markedly compressed the optic chiasm especially the right side (*white arrows*). *B–E*, Hyperintensity was recognized in the right optic nerve on T2-weighted image (*arrows*). *F–H*, Hyperintensiy in the right optic nerve lasted for 2 years after the tumor reduction (*arrows*).

asm and Wallerian degeneration in the ventral side of the optic chiasm.

With regard to VA disturbance caused by compression near the optic chiasm, several studies have reported that this was caused by optic chiasm compression from the internal carotid artery,[5,6] but few studies have compared imaging findings.[5-7] The present study on tumor-induced compression demonstrated a statistically significant correlation between disease duration and improvement in VA. We also showed that it is meaningful to be able to visually assess compression of the optic chiasm and optic nerves and accurately examine the optic nerves.

In the present study, signal intensity abnormality did not advance to the optic pathway posterior to the tumor, even in patients in whom compression advanced posterior to the optic chiasm. Moreover, tumor location in relation to the optic chi-

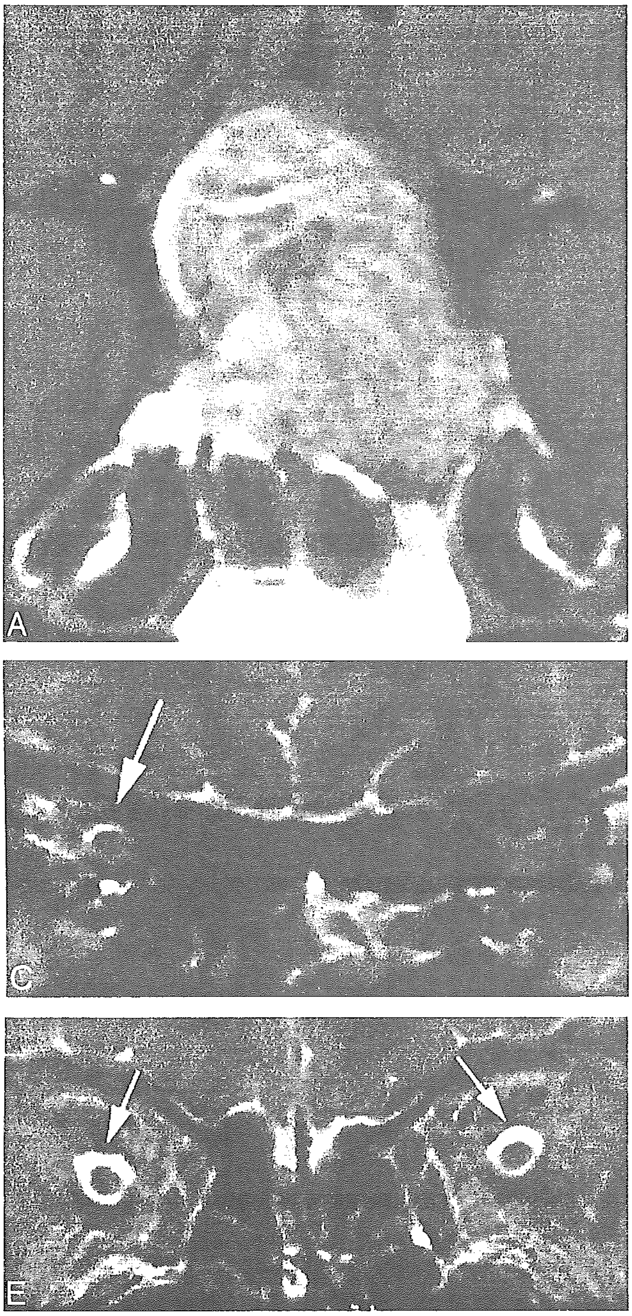

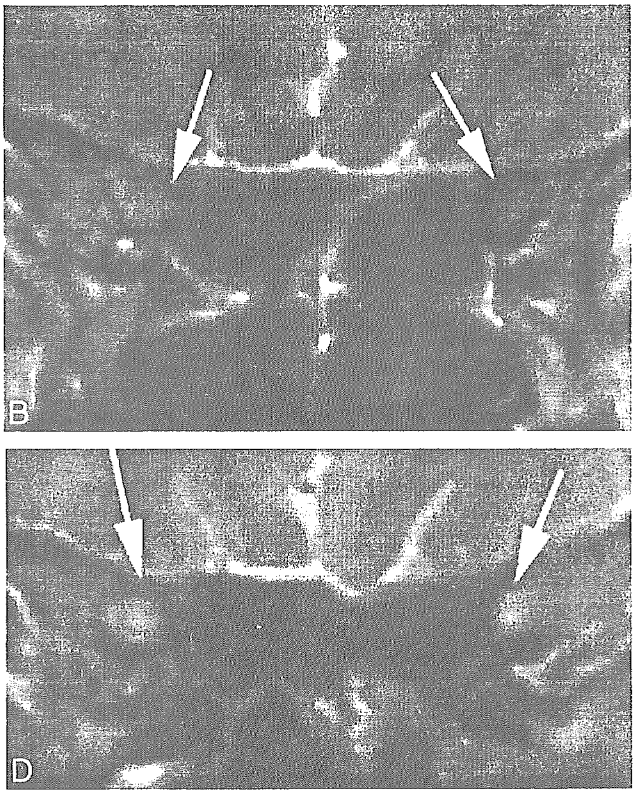

Fig 6. Case 17, a 58-year-old man, whose disease duration from the initial examination to the operation was 26 months. VA was not stable, though fixed VA disturbance was not recognized on the initial examination. *A*, Pituitary adenoma compressed the optic chiasm. *B*, Hyperintensiy of the optic nerve was not shown (*arrows*) on the initial examination. *C*, Right-side perioptic subarachnoid space dilated slightly on the initial examination (*arrow*). *D* and *E*, Tumor reduction was performed 26 months after the initial examination. Hyperintensity was shown in the bilateral optic nerve ventral to the optic chiasm (*D*, *white arrows*) and bilateral perioptic subarachnoid space dilated markedly (*E*, *white arrows*), probably representing atrophic change of the optic nerves.

asm and optic nerves exhibited no correlation to signal intensity abnormality. In craniopharyngioma arising in the suprachiasmal region, though, edema has been known to occur in the optic pathway posterior to a tumor, and, as a result, we believe that it will be necessary to further investigate the relationship of signal intensity abnormality to tumor location.

In case 17 (Fig. 6), only signal intensity abnormality of the perioptic subarachnoid space was initially observed, and, though VA was not stable, surgery was delayed for various reasons and optic atrophy eventually developed. In other words, signal intensity abnormality can lead to severe atrophy, which suggests the importance of performing surgery at an appropriate stage. Because VA improvement is closely correlated to disease stage, it is important to recommend expedient decompression.

VA disturbance was marked from the beginning in some patients despite mild compression. In one such patient (case 20), signal intensity abnormality was localized to the left prechiasmatic region and the perioptic subarachnoid space was enlarged, resulting in symptoms resembling acute optic neuritis. In this patient, pituitary apoplexy was suspected, and microhemorrhage could have caused chemical inflammation. Hence, optic nerve degeneration due to long-term compression was not the sole factor in VA impairment. In other words, it is necessary to assess etiology in each patient. Furthermore, in this patient, as a result of imaging findings and papillary edema, steroids were administered from an early stage, leading to an improvement in VA. This case emphasized the importance of carefully analyzing imaging findings.

References

1. Nagahata M, Hosoya T, Kayama T, et al. **Edema along the optic tract: useful MR findings for the diagnosis of craniopharyngiomas.** *AJNR Am J Neuroradiol* 1998;19:1753–57
2. Saeki N, Uchino Y, Murai H, et al. **MR imaging study of edema-like change along the optic tract in patients with pituitary region tumors.** *AJNR Am J Neuroradiol* 2003;24:336–42
3. Miller NR. **Tumors of the pituitary gland.** In: Walsh and Hoyt's clinical neuro-opthalmology. 4th ed. Philadelphia: Willliams and Wilkins; 1424–86
4. Hoyt WF. **Correlative function anatomy of the optic chiasm.** *Clin Neurosurg* 1970;17:189–208
5. Ogata N, Imaizumi M, Kurokawa H, et al. **Optic nerve compression by normal carotid artery in patients with normal tension glaucoma.** *Br J Ophthalmol* 2005;89:174–79
6. Kawasaki A, Puruvin VA. **Photophobia as a the presenting visual symptom of chiasmal compression.** *J Neuroophthalmol* 2002;22:3–8
7. Forooan R. **Chiasmal syndrome.** *Curr Opin Ophthalmol* 2003;14:325–31

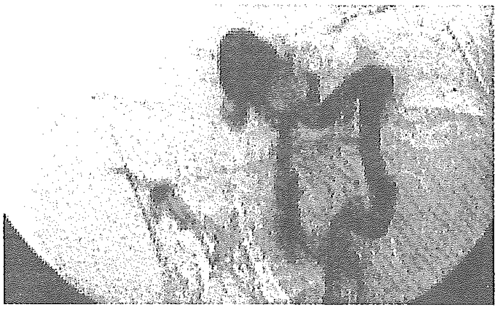

FIG. 2. – Opacification de l'artère vertébrale gauche. Incidence de profil. Fistule artério-veineuse vertébrale avec une ectasie veineuse (NB ballonnet dans le secteur veineux).

FIG. 2. – *Left vertebral angiogram, lateral view. Vertebral arteriovenous fistula with venous ectasia. (Note. Balloon in the venous compartment).*

le débit, mais sans toutefois exclusion du shunt. Le positionnement d'un second ballon au niveau de la zone de shunt n'était pas possible en raison du risque d'exclusion de l'artère vertébrale en amont de la fistule. L'amélioration de la symptomatologie clinique est observée mais le scanner cérébral de contrôle n'a pas été réalisé.

La FAVV est caractérisée par une communication anormale entre l'artère vertébrale ou une de ses branches et la veine correspondante dans leur portion extra-crânienne [8]. Elle est le plus souvent la conséquence d'un traumatisme direct accidentel ou iatrogène [2]. Moins fréquemment, elle peut être spontanée et survenir dans le cadre d'une pathologie artérielle pré-existante [1, 4]. Le mécanisme physiopathologique de la FAVV spontanée est mal connu. Il est démontré que la pression élevée dans l'artère facilite le passage du sang artériel dans la veine, avec baisse de la pression artérielle en aval de la fistule, ainsi qu'un ralentissement circulatoire par rapport au côté sain [3], cette spoliation peut être responsable des signes neurologiques déficitaires et d'épilepsie. La fistule entraîne une hyperpression veineuse qui diminue le gradient artério-veineux dans les territoires concernés, et donc la pression de perfusion tissulaire [1]. L'hydrocéphalie observée chez notre patient peut s'expliquer par une hyperpression veineuse gênant la résorption du liquide cérébrospinal. Encore faut-il s'interroger sur le caractère compressif de la fistule en se demandant s'il n'existe pas une association de facteur favorisant ? L'angiographie, examen-clé du diagnostic, permet de préciser les possibilités de traitement. Chez notre patient, bien que la fermeture de la fistule soit incomplète, une amélioration de la symptomatologie a été obtenue.

RÉFÉRENCES

[1] CLUZEL P, PIEROT L, LEUNG A *et al.* Vertebral arteriovenous fistulae in neurofibromatosis : report of two cases and review of literature. *Neuroradiology* 1994; *36:* 321-325.

[2] HALBACH VV, HIGASHIDA RT, HIESHIMA GB. Treatment of vertebral arterivenous fistula. *AJR Am J Roentgenol* 1988; *150:* 405-412.

[3] PERTUISET B, ANCRI D, ARTHUIS F *et al.* Shunt-induced haemodynamic disturbances in supratentorial arteriovenous malformations. *J Neuroradiology* 1985; *12:* 165-178.

[4] RIENHOFF WF. Congenital arteriovenous fistula. *John Hopkins Medical Bulletin* 1924; *35:* 271-286.

[5] SAINT-MAURICE JP, HOUDART E, Gelbert F *et al.* Malformations vasculaires vertébromédullaires. Encycl Méd Chir (Elsevier, Paris), Radiodiagnostic – Neuroradiologie – Appareil locomoteur, 31-671-G-10, 1998.

HYPERAMMONEMIC ENCEPHALOPATHY WITH BLUE RUBBER BLED NEVUS SYNDROME

A.M. TOKUMARU (1), I. SAKATA (2), H. TERADA (3), S. KOSUDA (2), S. YOSHIMITSU (4), S. NAGAO (4), T. AKIMA (5), M. MIZUNO (1), M. YAMAKAWA (1)

(1) Department of Radiology, Tokyo Metropolitan Hospital of Gerontology, 35-2 Sakae-cho Itabashi-Ku, Tokyo Japan 173-0015.
(2) Department of Radiology, National Defense Medical College, 3-2 Namiki-Cho Tokorozawa-City, Saitama Japan 359-8513.
(3) Second department of Radiology, Toho University School of Medicine, 2-17-6 Ohashi Meguro-Ku Tokyo, Japan 15308515.
(4) Department of 2nd Internal Medicine.
(5) Department of Pathology, National Defense Medical College, 3-2 Namiki-Cho Tokorozawa-City, Saitama Japan 359-8513.

We describe the case of a 40-year-old woman with hyperammonemic encephalopathy induced by blue rubber bled nevus syndrome (brbns).

The patient was admitted to our hospital with impaired consciousness accompanied by acute hyperammonemia due to a combination of factors, including long-term IVH management, chronic hepatic dysfunction due to repeated gastrointestinal hemorrhage, and portal-systemic shunting associated with brbns, as indicated by indirect findings at autopsy. On admission, T2-weighted MR images demonstrated bilateral hyperintense lesions in the insular cortices, bilateral cingulate gyri, and internal capsules, in addition to diffuse swelling of the subcortical white matter. T1-weighted images

---

Reprint request: A.M. TOKUMARU, address above.
e-mail: tokumaru@tmgh.metro.tokyo.jp

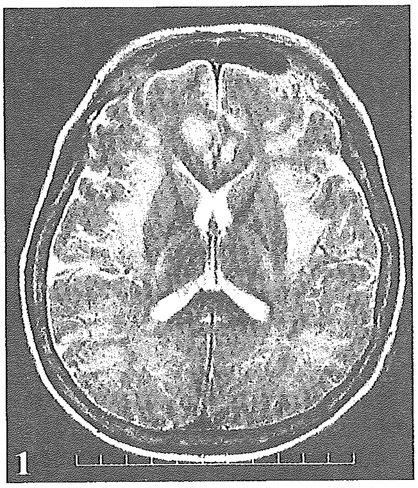

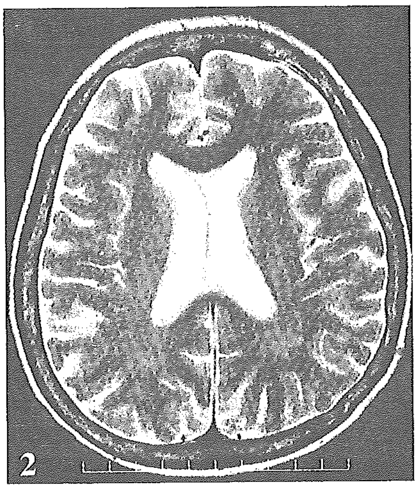

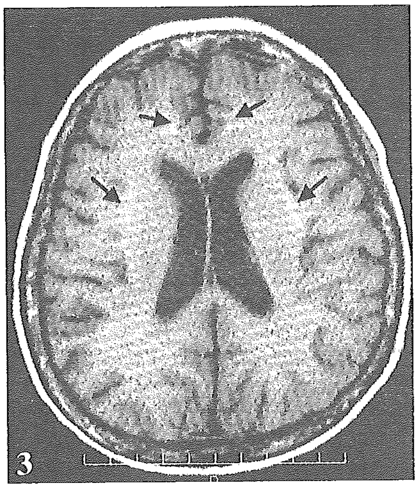

FIG. 1. – Axial T2 weighted image (TR/TE=3300/120) done on the 5th day of admission showing hyperintense lesions in the bilateral insular cortices, bilateral cingulated gyri, and bilateral internal capsules, and diffuse subcortical white matter swelling.

FIG. 1. – Coupe axiale. Séquence pondérée en T2 (TR/TE = 3300/120). IRM réalisée 5 jours après l'admission : lésions hyperintenses des cortex insulaires, des gyri cingulaires et des capsules internes. Gonflement cortical diffus.

FIG. 2. – Two weeks after admission, axial T2 weighted image (3300/120) showing interval resolution of abnormal signal intensity and swelling.

FIG. 2. – Coupe axiale. Séquence pondérée en T2 (TR/TE = 3300/120). IRM réalisée 2 semaines après l'admission. Disparition des anomalies.

FIG. 3. – T1 weighted image (550/15) showing new lesions of linear hyperintensity along the insular cortex and cingulate gyri (arrows). Symmetrical hyperintense lesions extending between globus pallidus and mesencephalon showed no significant interval changes.

FIG. 3. – Coupe axiale. Séquence pondérée en T1 (TR/TE = 550/15). Nouvelles lésions linéaires, hyperintenses, le long des cortex insulaires et des gyri cingulaires (flèche).

demonstrated symmetrical hyperintense lesions from the globus pallidus to the mesencephalon. Two weeks after admission, MRI showed abnormal signal intensity on T2-weighted images; however, swelling had resolved and clinical status improved. T1-weighted images showed new linear hyperintense lesions along the insular cortices and cingulate gyri.

While there have been reports of hyperammonemic encephalopathy caused by valproic acid therapy or pediatric metabolic disorders [1, 2, 6], to the best of our knowledge, the literature contains no reports of hyperammonemic encephalopathy caused by brbns. The present patient developed hyperammonemic encephalopathy due to various factors including gastrointestinal hemorrhage and hepatopathy accompanying brbns. MRI findings were useful in diagnosing hyperammonemic encephalopathy and in ascertaining its pathological features and following its pathologic course. While several studies have reported that the location of lesions differs between hyperammonemic encephalopathy induced by valproic acid and that in which this medication does not contribute [2], many researchers have found that swelling and abnormal signal are seen in the insular cortices and cingulate gyri regardless of underlying disease [1, 2]. Takanashi and colleagues reported three infants with proximal urea-cycle disorders, and concluded that secondary hypoperfusion was the cause of encephalopathy based on the location of lesions [6]. However, the degree of resistance to hypoperfusion differs between infants and adults, and further investigation is necessary to ascertain the effects of age-related factors and underlying disease.

The pathological features of hyperammonemic encephalopathy have been the subject of active discussion, and experiments have shown the involvement of edema. Furthermore, in the present patient, the MRI lesions disappeared and the hyperammonemic encephalopathy appeared to have mainly involved edema [3-5]. However, the new linear hyperintense lesions in the insular cortices and cingulate gyri seen on T1-weighted MRI that appeared when the clinical findings improved could have reflected laminar necrosis. Few MRI studies have followed patients with improved clinical findings, and laminar necrosis has been documented experimentally, but not by diagnostic imaging. Hence, the present case provides clinically meaningful information.

REFERENCES

[1] Arnold SM, Els T, Spreer J, Schumacher M. Acute hepatic encephalopathy with diffuse cortical lesions. *Neuroradiology* 2003; *43*: 551-554.

[2] Baganz MD, Dross PE. Valproic Acid-Induced Hyperammonemic Encephalopathy: MR Appearance. *AJNR* 1994; *15*: 1779-1781.

[3] Connelly A, Cross JH, Gadian DG *et al.* Magnetic resonance spectroscopy shows increased brain glutamine in orinithine transcarbamylase deficiency. *Pediatr Res* 1993; *33*: 77-81.

[4] McCandless DW, Schenker S. Effect of acute ammonia intoxication on energy stores in the cerebral reticular activating system. *Exp Brain Res* 1981; *44*: 325-330.

[5] Shcenker S, McCandless DW, Brophy E, Lewis MS. Studies on the intracerebral toxicity of ammonia. *J clin Invest* 1967; *46*: 838-848.

[6] Takanashi J, Barkobich AJ, Cheng SF, Weisiger K, Zlatunich CO, Mudge C *et al.* Brain MR Imaging in Neonatal Hyperammonemic Encephalopathy Resulting from Proximal Urea Cycle Disorders. *AJNR* 2003; *24*: 1184-1187.